<< Previous Chapter

PART IV

SOLUTIONS

In Part II of our book, we developed the equations governing radiative transfer in natural waters. In Part III we discussed three powerful methods for solving those equations: Monte Carlo, discrete-ordinates, and invariant imbedding methods. We are now – at long last – in position to solve the RTE and to investigate the nature of underwater light fields. The last part of our book therefore presents a selected set of numerically generated underwater light fields.

In Chapter 11 we shall study the behavior of the radiance, and of the various irradiances and apparent optical properties computed therefrom, for a selected set of inherent optical properties and external environmental conditions. In so doing, we shall develop intuition about the dependence of the various radiometric quantities and AOP's on the IOP's and boundary conditions typical of natural water bodies. In addition, we shall see the capabilities and limitations of such numerical models as tools for optical oceanography and limnology.

This Page Intentionally Left Blank

Chapter 11

Underwater Light Fields

The ideal next step in our study of light and water would be to study actual measurements of underwater spectral radiance distributions in conjunction with simultaneously measured water inherent optical properties and external lighting and boundary conditions. These measurements of course would be of high accuracy and cover the entire range of IOP's and boundary conditions found in nature. Unfortunately, such comprehensive data sets do not exist. In fact, there is not a single data set that includes both measured radiances and all IOP's at even one wavelength. Even the easily obtained irradiances are usually measured in conjunction with only a partial set of IOP's, typically the absorption coefficient at selected depths and wavelengths and the beam attenuation $c(z)$ at $\lambda = 660$ nm only. The phase function and incident sky radiance are almost never measured.

Such incomplete data sets are often satisfactory for the needs of oceanography and limnology. For example, in a study of phytoplankton productivity, it may be sufficient to measure depth profiles of PAR and $a_{\text{ph}}(\lambda)$ [the absorption by the phytoplankton], in conjunction with measurements of water temperature and salinity, nutrient availability, phytoplankton respiration, and so on. However, such data sets are of little value for the purpose of checking closure relations or testing the accuracy of radiative transfer predictive models. Nor, for example, can we study the detailed directional structure of underwater light fields if only irradiances are measured.

Lacking the desired measurements, the next best course of action is to numerically simulate underwater light fields using the methods of Part III. Although one good data set is worth a thousand poorly debugged computer programs based on incomplete physics, seeking recourse in numerical methods has certain advantages. After we have convinced ourselves that our numerical models are indeed providing accurate solutions of the RTE, these models can serve as ersatz controlled-environment laboratories. In numerical models – but not in nature – we have complete control over the IOP's and boundary conditions. We can at will "turn on" and "turn off" physical processes such as fluorescence, and thereby gain insight into the importance of such processes in nature. From an even more practical economic standpoint, a powerful desktop computer can be purchased for the

cost of one day of ship time. Moreover, placing our faith in computed quantities is often no less uncertain than placing our faith in measured values, when we recall the difficulties inherent in making certain measurements at sea.

In this chapter we therefore present several "case studies" based on numerically simulated underwater light fields. We shall not attempt to study comprehensively the full range of conditions found in nature for absorption, scattering, incident lighting, sea state, bottom conditions, and so on. However, a few carefully chosen simulations will highlight the salient features of underwater light fields. We shall resist the temptation to draw general conclusions from the few examples discussed here. We do present these simulations as illustrations of the type of numerical studies that can be carried out, from which generalizations can be made. These simulations will illustrate the power of numerical models and, we hope, inspire the reader to add such models to his or her collection of tools for the study hydrologic optics.

Our first task is to convince ourselves that the models are trustworthy.

11.1 Model Validation

The true test of a numerical model is to compare its predictions with carefully made measurements of the predicted quantity. But as already noted, the requisite comprehensive data sets containing all IOP's, environmental conditions, and radiometric quantities do not exist. Partial data sets do exist and will be discussed. However, our first interest is in comparing the different numerical methods.

Model-model comparison

Mobley, *et al.* (1993) compared in detail seven numerical models now in routine use in optical oceanography. These models included an invariant imbedding model based on the equations summarized in Figs. 8.1 and 8.2, a discrete-ordinates model, and five Monte Carlo models of varying degrees of sophistication. This study found that any of these numerical models provides a solution of the RTE that is sufficiently accurate for most of the needs of optical oceanography. We shall only illustrate the kind of model comparisons mode, in order to show their consistency.

Consider the following simulation of a natural water body. We take the phase function to be the average particle phase function $\tilde{\beta}_p$ as seen in

Fig. 3.13 and in Table 3.10. The albedo of single scattering is $\omega_o = 0.9$; this represents highly scattering water. The air-water surface is taken to be level; the index of refraction of the water (relative to the air) is $n_w = 1.34$. These IOP's are all independent of depth. The sun is an infinitely distant point source located at a zenith angle of $\theta_s = 60°$. The solar irradiance just above the sea surface is taken to be $E_\perp = 1.0$ W m^{-2} nm^{-1} on a surface perpendicular to the sun's direct beam; this is equivalent to $E_d(a) = 0.5$ W m^{-2} nm^{-1}. The sky is otherwise black. There are no internal sources or inelastic scattering within the water body. The water is infinitely deep.

These stipulations uniquely define the IOP's and boundary conditions of the problem, so that a unique solution of the RTE (5.24) can be obtained. Note that it is not necessary to specify the absorption and scattering properties individually, only their ratio as seen in $\omega_o = b/(a+b)$. Likewise, the beam attenuation is not needed as long as we express the solution radiance as a function of optical depth ζ. The radiance $\boldsymbol{L(\zeta;\theta,\phi;\lambda)}$ is valid for any wavelength λ that has IOP's equal to the stated values. Reference to Tables 3.4 and 3.10 shows that our choice of IOP's is consistent with $\lambda = 550$ nm and very turbid water containing, perhaps, resuspended sediments to give unusually high scattering.

Figure 11.1 shows radiances in the plane of the sun at three optical depths, as computed by three entirely different numerical methods: invariant imbedding, discrete ordinates, and Monte Carlo. We shall discuss this figure in detail presently, but for now the main feature to be noted in the figure is that the solid, dashed, and dotted lines corresponding to the three numerical models are virtually indistinguishable. In other words, *it does not matter which of these numerical methods is used; each gives the same solution for the RTE.* If the computed radiance distributions are identical, then so are the irradiances and all apparent optical properties. The small discrepancies that can be seen in the figure result from the different directional discretizations used in the three models.

There are, however, *significant differences in the computational expenses associated with different numerical methods*. Table 11.1 shows the actual execution times used in computing the radiances shown in Fig. 11.1. Several important points must be kept in mind regarding these times. First, note that invariant imbedding was almost four times faster than discrete ordinates, and 800 times faster than Monte Carlo, when the relative computer speeds are taken into account. However, for much oceanographic work, only irradiances are required. In such cases, the discrete-ordinates method needs to solve only the $l = 0$ version of Eq. (9.20); computing only the irradiances required just 9 s in the present simulation. Likewise, the Monte Carlo model was severely tested in this simulation because of the

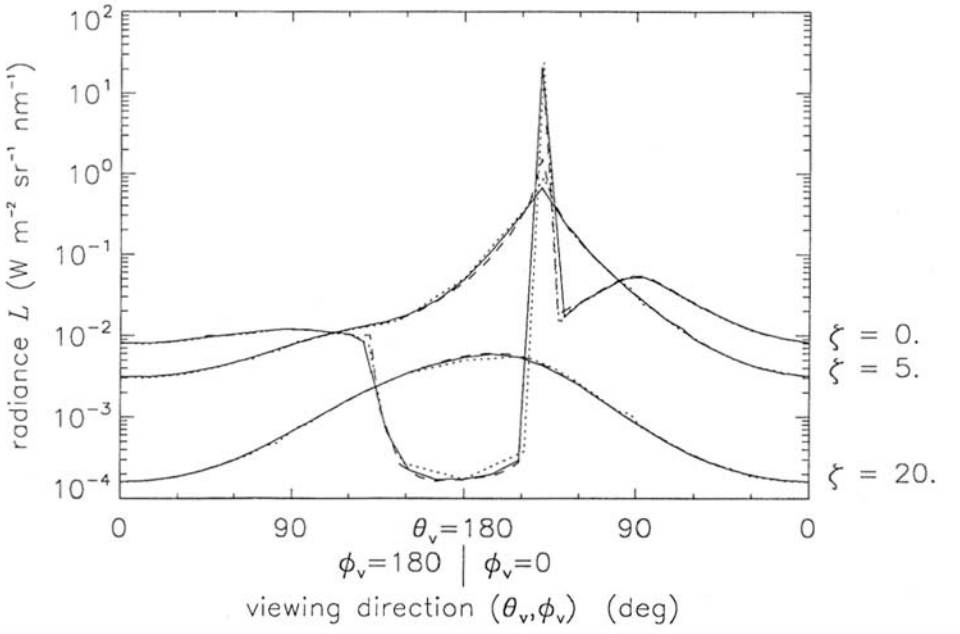

Fig. 11.1. Model-model comparison. The curves are radiances in the plane of the sun as computed by three numerical methods: invariant imbedding (solid line), discrete ordinates (dashed line, data courtesy of K. Stamnes), and Monte Carlo (dotted line, data courtesy of A. Morel). The simulation is defined and discussed in the text.

Table 11.1. Computer times required for the simulation underlying Fig. 11.1.

numerical method	computer used	computer speed (MFLOPS[a])	execution time (s)
invariant imbedding	Sun SPARCstation 2	3	496
discrete ordinates	Decstation 5000/240	12	435
Monte Carlo	Hewlett Packard 9000/730	27	45000

a. MFLOPS = Million Floating Point Operations Per Second

large number of simulated photons required in order to reduce the statistical fluctuation to a negligible level at 20 optical depths. Far fewer photons are required to compute only the irradiances, or to compute radiances at shallow depths only (as might be sufficient for remote sensing studies).

If the IOP's vary with depth, the discrete-ordinates model must resolve the water column as a number of homogeneous layers. The overall solution is obtained by matching the separate solutions for each layer at the layer boundaries; this increases the computer time dramatically. In one simulation requiring 25 layers, the discrete ordinates model required 19 times as long to compute the irradiances as in a homogeneous-water case [see Mobley, *et al.* (1993) for details]. A corresponding increase in the time required to compute a full radiance distribution can be expected. Thus, for inhomogeneous waters, the discrete ordinates method is much slower than invariant imbedding, whose run time is almost independent of the depth dependence of the IOP's. Based on considerations such as these, we can make the following rough statements:

- For general computations of radiance distributions at depth within plane-parallel but otherwise inhomogeneous waters (especially those with wind-blown surfaces), invariant imbedding is the preferred method.

- For irradiance computations in homogeneous waters, discrete ordinates is the fastest method. Discrete ordinates becomes much slower in highly stratified waters.

- Monte Carlo methods are competitive with invariant imbedding and discrete ordinates only for irradiance computations, and for radiance computations at shallow depths.

Standard radiance display

Throughout the remainder of the chapter, we shall plot cross-sections of radiance distributions as in Fig. 11.1. It is therefore worthwhile discussing this figure in more detail. The layout of the figure is as follows. For a given depth ζ, the radiance is plotted as a function of the *viewing direction* (θ_v,ϕ_v). This is the direction that an instrument points in order to detect photons traveling in the $\theta = 180° - \theta_v$ and $\phi = 180° + \phi_v$ direction. The azimuthal viewing angle θ_v is measured from the nadir $(+\hat{\boldsymbol{i}}_3)$ direction, just as is the photon direction θ. Likewise, both ϕ_v and ϕ are measured

from the downwind ($+\hat{\boldsymbol{i}}_1$) direction. Thus, $\theta_v = 0°$ in Fig. 11.1 means that we are looking straight down and seeing photons heading straight up ($\theta = 180°$); $\theta_v = 180°$ is looking straight up. If the sun is located downwind, $\phi_v = 0°$ means that we are looking toward the sun and seeing photons headed away from the sun ($\phi = 180°$). We shall use this standard plotting format throughout this chapter.

Returning now to Fig. 11.1, let us consider the curves for $\zeta = w = 0$, which is just below the calm water surface. Looking straight downward ($\theta_v = 0°$), we see the zenith (or nadir-viewing) radiance $L(\zeta=0;\theta_v=0,\cdot) \approx 0.0082$ W m^{-2} sr^{-1} nm^{-1}. As we raise our heads, looking away from the sun (the $\phi_v = 180°$ half-plane), the radiance increases slightly toward the horizon at $\theta_v = 90°$. This increase is a consequence of total internal reflection of photons that have been backscattered into nearly horizontal directions.

As we raise our heads further, there is a sudden drop in radiance near the critical angle for total internal reflection, $\theta_v \approx 132°$. When we look zenithward of the critical angle, we are looking within the "Snell circle" or "optical manhole," which is illustrated in Fig. 11.2. The entire sky hemisphere is mapped into the 48° Snell circle by the refractive effects of the air-water surface. Because we have simulated a black sky in the present instance, there is no sky radiance being transmitted through the surface into downwelling directions. The radiance within the Snell circle is therefore less than the diffuse radiance of the water in directions outside the Snell circle.

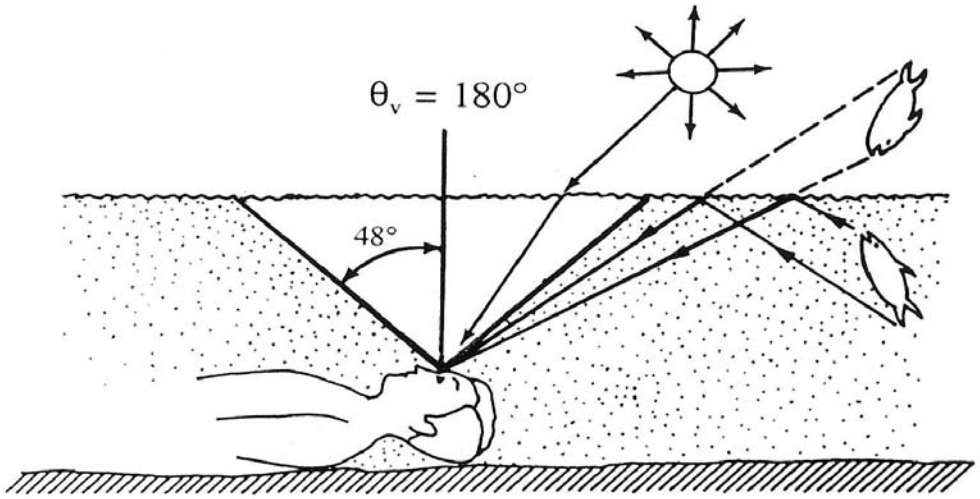

Fig. 11.2. Illustration of the Snell circle, or optical manhole. [redrawn from *H.O. I*]

When we are looking straight up ($\theta_v = 180°$), we are seeing only those photons that originally were heading straight upward at $\zeta = 0$, and which were reflected back downward by the underside of the air-water surface. Note (with the help of the digital output from the model run) that $L(\zeta=0;\theta_v=180°)/L(\zeta=0;\theta_v=0) = 1.727\times10^{-4}/8.236\times10^{-3} \approx 0.021$, which is precisely the Fresnel reflectance for normal incidence and $n_w = 1.34$; recall Eq. (4.14b). No photons are being transmitted through the surface and into the nadir direction because the sky is black and the surface is level.

We next look past the zenith and into the $\phi_v = 0$ half plane. When the viewing angle reaches $\theta_v \approx 140°$, we suddenly see the intense radiance of the sun's refracted beam. The angular width of the sun's spike as drawn in the figure is determined by the quad resolution (or an equivalent angular discretization). For example, the plotted output of the invariant imbedding model is the values of the quad-averaged radiances plotted at the θ_v values of the quad centers. In this simulation, there were quad centers located at θ_v = 151.6°, 139.7° and 127.7°. The other models had similar (but not identical) θ_v spacing near the sun's refracted direction. As our gaze moves past the sun, the radiance drops again. The prominent local maximum at $(\theta_v,\phi_v) = (90°,0°)$ results from photons being forward scattered into nearly horizontal directions and then undergoing total internal reflections. Looking past the horizon, the radiance decreases until we are once again looking straight down, at $\theta_v = 0$.

It is worth a moment's pause to perform a quick analysis of the plotted value of the sun's refracted beam just below the surface. Because the sky is black and the surface is level, the surface boundary conditions are easily comprehended. The quad-averaged boundary condition (4.67) reduces to just

$$\begin{aligned} L^+(w;u,v) &= L^-(w;r,s)\, r(w,a;r,s\to u,v) \\ &+ L^+(a;p,q)\, t(a,w;p,q\to u,v)\,. \end{aligned} \tag{11.1}$$

As in Chapter 8, the "+" and "−" superscripts on L remind us of the hemisphere containing the quad in question; $\Xi_d = \Xi_+$ or $\Xi_u = \Xi_-$. Here Q_{uv} represents the quad whose downwelling radiance ($Q_{uv} \in \Xi_+$) is plotted at (θ_v,ϕ_v) = (139.7°,0°) in Fig. 11.1. Q_{rs} is the quad in Ξ_- whose upwelling radiance is specularly reflected into Q_{uv}. Q_{pq} in Ξ_+ is the quad containing the sun's collimated beam; Q_{pq} is refracted through the surface into Q_{uv}. The locations and solid angles of these quads are shown in Table 11.2. The sun's input quad Q_{pq} has a small solid angle because the quad partitioning for this simulation was chosen to give a $\Delta\theta = 2°$ resolution near the sun's zenith angle. [This output is extracted from Mobley, *et al.* (1993), for

Table 11.2. Quad information for analysis of Eq. (11.1).

quad	center θ (deg)	center μ	solid angle (sr)
Q_{pq}	60.00	0.500	0.0079
Q_{rs}	40.26	0.763	0.0293
Q_{uv}	40.26	0.763	0.0293

which an *ad hoc* quad partitioning was used.] The quad-averaged value of the sun's radiance incident onto the air water surface is computed as

$$L^{+}(a;p,q) = \frac{E_{\perp}(a)}{\Omega_{pq}} = \frac{1.0 \text{ W m}^{-2} \text{ nm}^{-1}}{0.0079 \text{ sr}} = 126.36 \text{ W m}^{-2} \text{ sr}^{-1} \text{ nm}^{-1}.$$

(We have referred to the digital output for an accurate value of the final quantities.)

The radiance transfer function $t(a,w;p,q\rightarrow u,v)$ was computed using Monte Carlo ray tracing as described in Section 4.7. The radiant-power transfer function $\Phi^{++}(p,q\rightarrow u,v)$ of Eq. (4.68d) has the value 0.9403. Thus, 94.03% of the power originally in Q_{pq} is refracted through the surface into Q_{uv}; the remaining 5.97% is reflected upward by the surface. The value 0.9403 is just the average Fresnel transmittance of all the rays randomly initiated with $\hat{\xi}' \in Q_{pq}$ and refracted into direction $\hat{\xi} \in Q_{uv}$. The actual quad-averaged radiance transfer function $t(a,w;p,q\rightarrow u,v)$ is computed via Eq. (4.74b), using values from Table 11.2:

$$t(a,w;p,q\rightarrow u,v) = \Phi^{++}(p,q\rightarrow u,v) \frac{|\mu_p|\Omega_{pq}}{|\mu_u|\Omega_{uv}}$$

$$= 0.9403 \frac{|0.500|\ 0.0079}{|0.763|\ 0.0293} \approx 0.16618.$$

Likewise, we find $r(w,a;r,s\rightarrow u,v) = 0.06714$. The upwelling radiance $L^{-}(w;r,s)$ as computed from the full solution of the RTE as described in Chapter 8 is $L^{-}(w;r,s) = 0.01453$. Equation (11.1) thus yields

$$L^{+}(w;u,v) = (0.01453)(0.06714) + (126.36)(0.16618)$$

$$\approx 21.00 \text{ W m}^{-2} \text{ sr}^{-1} \text{ nm}^{-1}.$$

This is the value plotted in Fig. 11.1 at $\zeta = 0$ in the sun's direction. When the surface is not level, or when the sky is not black, Eq. (4.67) retains its sums over all quads and the analysis is more complicated. We shall not discuss the details of such situations.

At optical depth $\zeta = 5$ in Fig. 11.1, scattering within the water has greatly broadened the radiance maximum in the sun's direction, and the "black-sky effect" of reduced radiance seen within the Snell circle has been completely obliterated by light scattered downward within the water. By $\zeta = 20$, the radiance distribution is very near to the asymptotic distribution $\boldsymbol{L}_{\infty}(\theta_v)$, which is shown as the top curve of Fig. 9.3. We shall discuss the depth development of the radiance in more detail in Section 11.2.

Further model-model comparisons of this type, including surface, sky, and bottom effects; depth-dependent IOP's; and Raman scattering can be seen in Mobley, *et al.* (1993).

Model-data comparison

We now have convinced ourselves that the numerical methods of Part III all give the *same* answer. It remains to show that they also give the *correct* answer. This is more difficult because of the previously mentioned lack of comprehensive data sets with which to test the models.

One of the few data sets containing a complete underwater radiance distribution was acquired by Tyler and coworkers in Lake Pend Oreille, Idaho, USA on 22 April 1957 (Tyler, 1960). They measured $\boldsymbol{L}(z;\theta,\phi;\lambda)$ at seven depths from $z = 4.24$ m to $z = 66.1$ m; at 10° θ intervals from nadir to zenith; at 20° ϕ intervals; and in a broad wavelength band from 440 to 540 nm, with peak spectral response at $\lambda = 480$ nm. Measurements at one depth required about half an hour. Measurement of L started at 0852 and ended at 1441 local time. During this period the solar zenith angle changed from $\theta_s = 49°$ to 34.5° (at solar noon) to 47.5°. The solar azimuthal angle changed by 124° during the measurements. Considerable data massaging was performed in order to obtain a data set that is approximately equivalent to what would have been obtained at one particular solar angle; the details of the data reduction can be seen in Tyler's report. The day was crystal clear and windless; the water surface remained glassy calm throughout the measurement period. The water was almost homogeneous: $c(\lambda{=}480)$ varied from 0.397 m^{-1} at the surface to 0.382 m^{-1} at $z = 66$ m.

Unfortunately, however, no IOP's other than beam attenuation were measured, nor was the sky radiance, or even the total sky irradiance, measured. Therefore, in order to simulate the Tyler data with a numerical model, we will have to make some educated guesses about the remaining IOP's and input radiance. We can start by assuming that the average particle phase function $\tilde{\beta}_p$ of Fig. 3.13 and Table 3.10 is applicable. We can take the water as homogeneous with $c = 0.4\ m^{-1}$; this allows us to convert optical depth to geometric depth. However, we do not know the individual contributions of a and b to c, so we do not know ω_o. Let us take a wild guess and use $\omega_o = 0.7$, which is a typical value for a natural water body. Because the sky was free of haze or clouds, let us assume that 90% of the incident irradiance came from the sun's direct beam, and that the remaining 10% came from a uniform background sky. Let us place the sun in a quad centered at a zenith angle of $\theta_s = 38°$. Finally, we take the surface as level (zero wind) and the bottom as infinitely deep.

If you think that these assumptions make the model-data comparison somewhat questionable, you are quite correct. We see here the perfect example of the problems encountered in trying to achieve model closure, as discussed in Section 3.12.

In order to simulate the Tyler data, the invariant imbedding model of Chapter 8 was run with the "equal $\Delta\theta$" quad partition seen in Fig. 4.19b. The sun was therefore "smeared out" over the region $33.2° \le \theta_s \le 42.6°$ and $352.5° \le \phi_s \le 7.5°$. This quad resolution is coarser than the 3.3° acceptance angle (angle α in Fig. 1.5) of Tyler's radiance meter. Because Tyler reported only relative radiances, we normalized both data and model to their respective values of $L(z = 4.3\ m; \theta_v = 0°, \cdot)$, the upwelling radiance nearest to the water surface (i.e., all radiances were divided by this value).

The diamonds in Fig. 11.3 show some of the normalized Tyler data in the plane of the sun's rays, at three depths. The solid lines show the corresponding model predictions. The model-data agreement is generally quite good. The main discrepancies are near the surface in the viewing direction of the sun's refracted image. These differences are attributable to the differences in the sun's true position and its quad-averaged position, and to the unknown errors in the assumed input values.

We can view this good agreement in either of two ways. On the one hand, it is nothing short of miraculous, considering the number of assumptions made by Tyler in cleaning up the raw data and by us in running the numerical model. The good agreement is probably beginner's luck, and we should quit while we are ahead. On the other hand, the good agreement is meaningless and trivial, because with so many free parameters in the model, we can bring its predictions into good agreement with any data set.

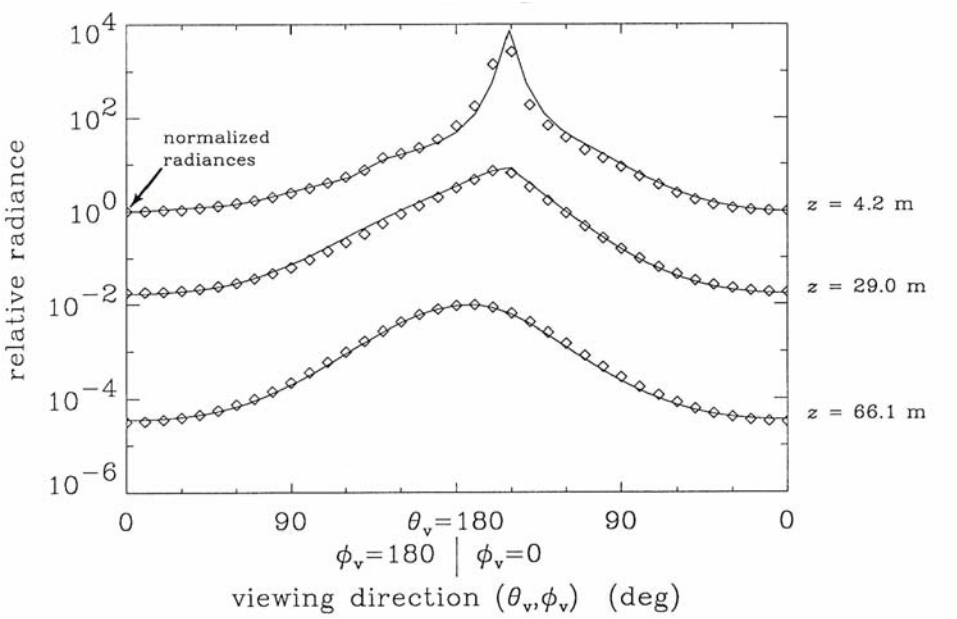

Fig. 11.3. Model-data comparison. The diamonds are relative radiances measured by Tyler (1960) under clear-sky, calm-surface conditions, and the solid lines are the corresponding model predictions.

This comparison is perhaps best viewed as a reassuring check on the model's ability to simulate underwater light fields, but the comparison cannot be viewed as an absolute check on the model's correctness.

Now that we have seen Fig. 11.3, a confession must be made. Our first "wild guess" for ω_o was $\omega_o = 0.5$, which is also a reasonable value for natural waters. This value caused the radiance to decrease too rapidly with depth, relative to the normalized values at $z = 4.2$ m. Moreover, the near-asymptotic distribution at $z = 66.1$ m had the wrong shape (θ_v dependence): recall from Fig. 9.3 how $\boldsymbol{L}_\infty(\theta_v)$ depends on ω_o. On the second attempt, we increased ω_o to 0.7, which gives relatively less absorption and thus more light reaching a given depth. The value of $\omega_o = 0.7$ gives both the correct magnitude and the correct shape for $L(z{=}66.1;\theta_v,\phi_v)$. But note that in adjusting the value of ω_o, albeit by trial and error, *we have solved an inverse problem*! In particular, *we have recovered the value of* ω_o *from in situ radiance measurements*. Our solution was obtained by a sequence of (two) direct solutions; this is an implicit solution as discussed in Section 10.1. The recovered value of $\omega_o = 0.7$ and the measured value of $c = 0.4$ m^{-1}

together yield $a = 0.12$ m^{-1} and $b = 0.28$ m^{-1}. The correctness of these recovered ω_o, a and b values of course depends on the correctness of the underlying assumptions about the shape of $\tilde{\beta}$, and so on.

Tyler also measured the radiance when the sky was heavily overcast. We shall compare our model with those data in Section 11.3.

In spite of our inability to achieve rigorous model closure, comparisons such as those seen here convince us that the numerical models now in use in optical oceanography and limnology are indeed correctly predicting underwater light fields, at least to first-order accuracy. Processes omitted from various models, e.g. fluorescence and Raman scattering, polarization, and surface-gravity-wave effects, can at times be important. The limitations of particular models therefore must be kept in mind when interpreting their predictions. Nevertheless, we can proceed with confidence in the simulations for this chapter.

11.2 Depth Development of the Radiance Distribution

We saw in Fig. 11.1 that the radiance underwent a great transformation of its directional distribution between the surface and five optical depths. We now consider this near-surface behavior of underwater light fields in more detail.

For concreteness, let us simulate the same homogeneous, source-free, infinitely deep water body that was used to generate Figs. 9.5 and 9.6. This water is described by the average particle phase function $\tilde{\beta}_p$, and by either $\omega_o = 0.8$ (high scattering) or $\omega_o = 0.2$ (high absorption). The equal $\Delta\theta$ quad partition of Fig. 4.19b is used. We shall place the sun in the quad centered at a zenith angle of $\theta = 57°$ (see Table 4.1). The sky is otherwise black. The total input irradiance on a plane perpendicular to the sun's rays is $E_\perp = E_{od} = 1$ W m^{-2} nm^{-1}, which for a black sky is entirely due to the sun's direct beam. The water surface is level, and the bottom is infinitely deep. We shall consider variations on this scenario in the next several sections.

Figure 11.4(a) shows a cross-section of the radiance in the plane of the sun for the case of $\omega_o = 0.8$. The plot shows the radiance profile every 0.1 optical depths from $\zeta = 0.0$ to $\zeta = 0.5$, and at depths $\zeta = 1$, 2, 5, and 10. Figure 11.4(b) shows a cross-section in the plane perpendicular to the sun's rays. This cross section does not see the bright sun; note the change in ordinate scale. The feature to note in either figure is the rapid "filling in"

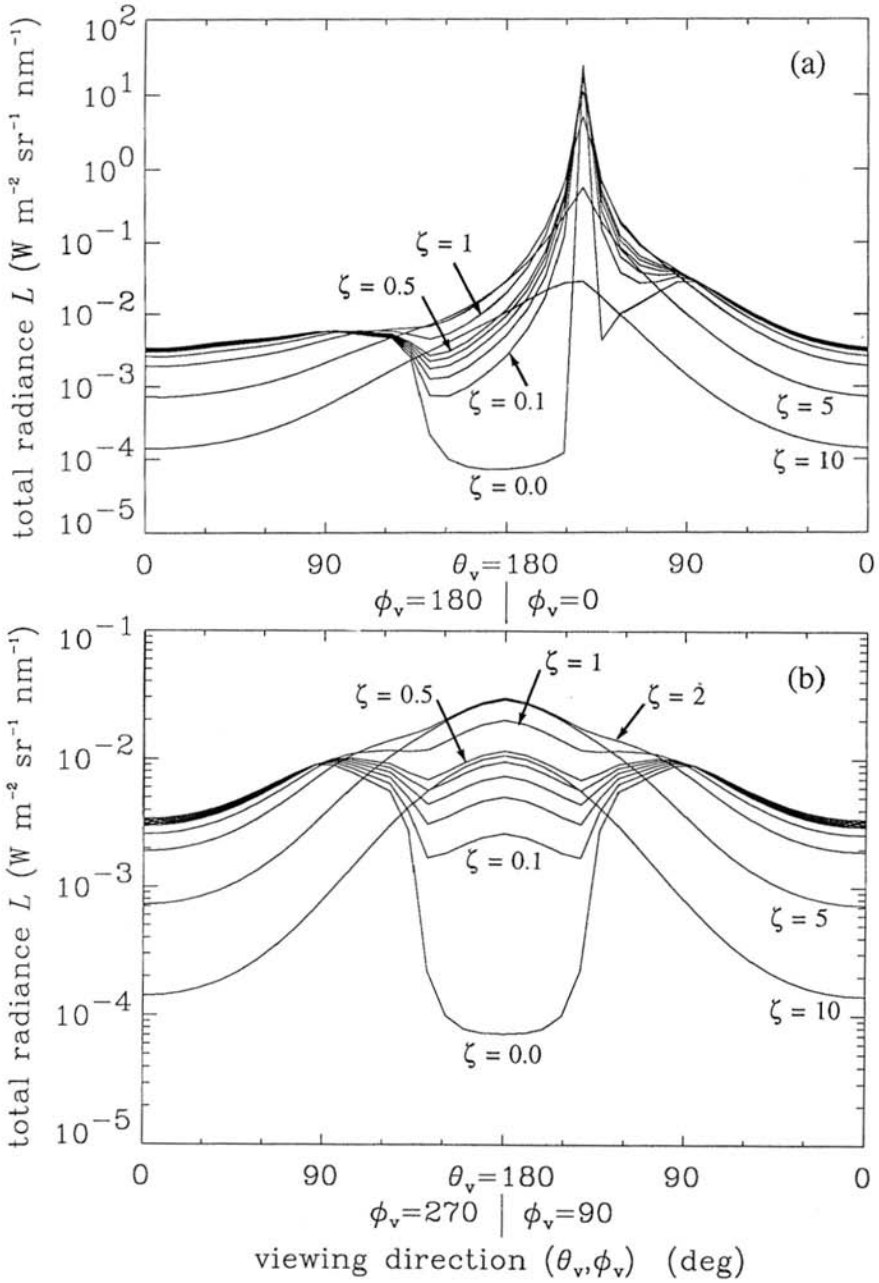

Fig. 11.4. Radiances plotted in the plane of the sun's rays (panel a) and in the plane perpendicular to the sun's rays (panel b), for various optical depths ζ. The sky was black and the solar zenith angle was $\theta_s = 57°$.

of the "dark-sky effect" seen when looking within the Snell circle, i.e., when θ_v is near 180°. The origin of this effect was explained in the discussion of Fig. 11.1. The feature has almost disappeared by one optical depth, and is completely gone by $\zeta = 2$, in this highly scattering water.

Next note the depth dependence of the nadir (zenith-viewing) radiance $L_d(\zeta) \equiv L^+(\zeta;\theta=0,\cdot)$, which is plotted at θ_v=180°. Just below the surface, $L_d(\zeta=w) = 7.2\times10^{-5}$ W m^{-2} sr^{-1} nm^{-1}. L_d increases rapidly to 2.6×10^{-3} at ζ = 0.1 and continues to increase until $\zeta \approx 3.5$ (not shown), when it reaches a value of $L_d \approx 3.3\times10^{-2}$. As we go deeper, L_d begins to decrease; its value is $L_d \approx 1.1\times10^{-2}$ at ζ = 10. The zenith (nadir-viewing) radiance $L_u(\zeta) = L^-(\zeta;\theta=180°,\cdot)$, which is plotted at $\theta_v = 0°$, decreases monotonically with increasing depth: $L_u(\zeta=w) \approx 3.4\times10^{-3}$ and $L_u(\zeta=10) \approx 1.4\times10^{-4}$. This behavior in L_d and L_u is exactly what was seen in Fig. 5.3, which was drawn from Tyler's Lake Pend Oreille data. The discussion of Fig. 5.3 in Section 5.9 should be reviewed.

Although the sky was of course not dark when Tyler took his data, it was relatively dark compared to the brilliant sun, and the effect showed up in his measurement just below the surface, as seen in Fig. 5.3. No hint of a dark-sky effect is seen in his data at depth z = 4.2 m, as seen in Fig. 11.2. This depth corresponds of an optical depth of $\zeta = cz$ = (0.4 m^{-1})× (4.2 m) = 1.7, which is deep enough for the effect to have disappeared completely. Let us recapitulate the discussion from Section 5.9. Very near the surface, where the nadir radiance is small because of the dark sky, forward scattering from the solar beam (through angles ψ ~ 40°) is adding more photons to the nadir direction than absorption is removing, and L_d increases with depth. Deeper in the water, the solar beam becomes weaker, absorption becomes the dominant radiative process, and L_d begins to decrease. Absorption always wins, if we go deep enough.

The main idea illustrated in Fig. 11.4 is that a lot can happen, optically speaking, within the first optical depth. Features such as the rapid filling of the black-sky effect can be measured if conditions are right, as they were on the calm day in Lake Pend Oreille. However, such effects are seldom observed in actual field experiments. Irradiance measurements integrate out the angular structure of the radiance distribution, which minimizes such effects. As we shall see in the next sections, a bright sky and surface waves obliterate interesting directional features. And, finally, oceanographers seldom make measurements very near the sea surface. It is rather hard to measure a full radiance distribution at, say, z = 0.1 m, when the ship is being rocked by waves 2 m high.

Figure 11.5 illustrates the more gradual change in radiance distributions at depths greater than ζ ~ 1. Panel (a) of the figure shows the

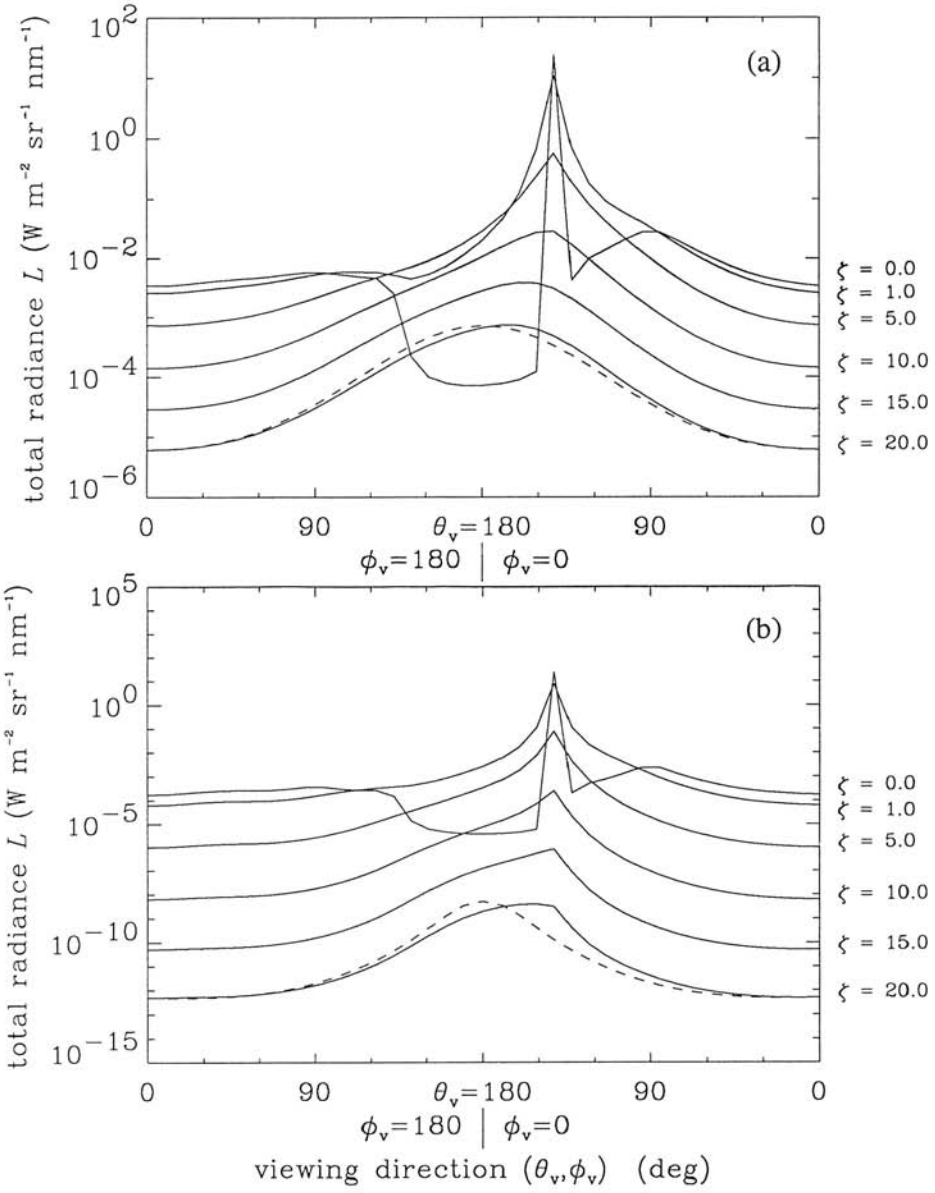

Fig. 11.5. Panel (a) shows the radiance distribution for the same $\omega_o = 0.8$ case that was simulated in Fig. 11.4(a); the radiances are now displayed to 20 optical depths. Panel (b) is identical except that $\omega_o = 0.2$. In each panel, the dashed line is the asymptotic distribution $L_\infty(\theta_v)$ scaled by $L(\zeta=20;\theta_v=0)$.

same situation as Fig. 11.4(a), but now the radiance is plotted at depths $\zeta = 0$, 1, 5, 10, 15, and 20. The dashed line shows the shape of the asymptotic distribution $L_\infty(\theta_v)$, scaled to the value of $L(\zeta=20;\theta_v=0)$. The actual radiance and its scaled asymptotic shape differ by at most a factor of 1.4 at 20 optical depths, for this case with $\omega_o = 0.8$. Panel (b) of the figure shows the same situation as panel (a), except that now $\omega_o = 0.2$. Note that the position of the sun is still discernable at $\zeta = 20$, even though the magnitude of the radiance at $\zeta = 20$ is much less than the corresponding magnitude seen in panel (a). The scaled asymptotic distribution now differs from the actual $L(\zeta=20;\theta_v)$ by as much as a factor of 24. The radiance for the $\omega_o = 0.2$ case is approaching its asymptotic form much more slowly than was the case for $\omega_o = 0.8$. We already have seen this behavior expressed in terms of the *K*-functions in Figs. 9.5(a) and 9.6(a). Figure 11.5 shows us the radiance behavior that underlies the previously discussed *K*-function behavior.

11.3 Sky Effects

The black-sky situation modeled in the previous section is a limiting case that is useful for pedagogic purposes, but which is not a good approximation of sky conditions in nature. Therefore, we next investigate the effects of the sky radiance distribution on underwater radiances, irradiances, and apparent optical properties.

Let us again consider the $\omega_o = 0.8$, level-surface water body. We keep the sun in the quad centered at $\theta_s = 57°$, and we keep the total incident irradiance $E_{od}(a)$ equal to one. In the black-sky simulation of the last section, all of $E_{od}(a)$ was due to the sun's collimated beam. Now we let $E_{od}(a)$ be partitioned as a fraction f_s ($0 \le f_s \le 1$) due to diffuse radiance from the sky itself, and a fraction $1 - f_s$ due to the direct solar beam. Thus

$$f_s \equiv \frac{E_{od}(\text{sky})}{E_{od}(\text{sky}) + E_{od}(\text{sun})} . \tag{11.2}$$

The background sky radiance is taken to be a cardioidal distribution, as given by Eq. (1.35).

Figure 11.6 shows the radiance as a function of f_s, in the plane of the sun, just below the surface at $\zeta = w = 0$. The curve for $f_s = 0$ is the same $\zeta = 0$ curve seen in Figs. 11.4(a) and 11.5(a). The curve for $f_s = 0.01$ shows that if only 1% of the total irradiance is from the sky, then the black-sky effect is lost. For $f_s = 0.1$ an underwater observer sees a radiance within the

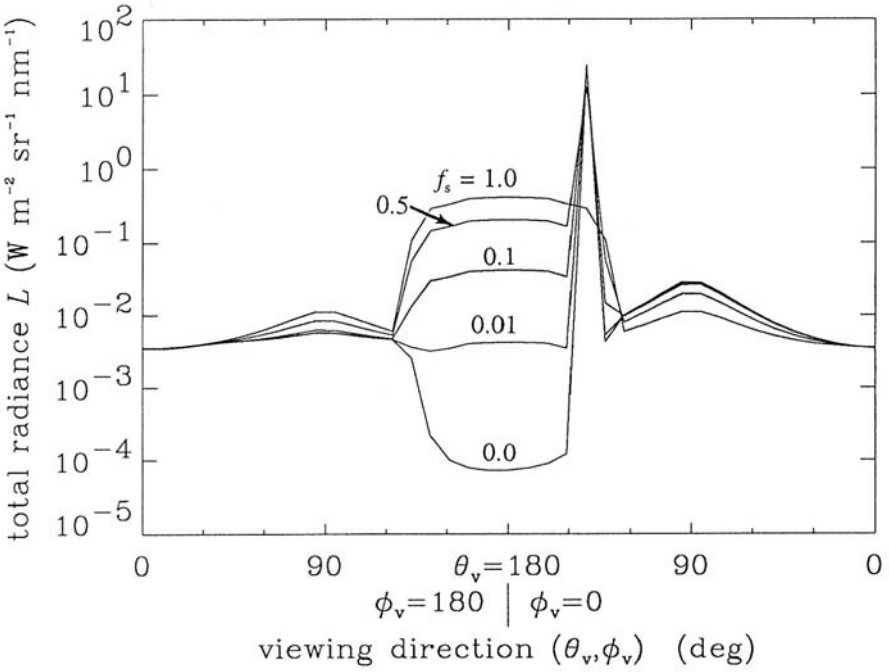

Fig. 11.6. Computed radiance profiles just below the surface, for different ratios f_s of sky to total incident irradiance; $f_s = 0$ is a black sky and $f_s = 1$ is a heavily overcast sky with no discernable sun.

Snell circle that is an order of magnitude greater than the radiance outside the Snell circle. Excellent photographs of precisely this effect, made with a fisheye lens, can be seen in Smith (1974; his Figs. 2 and 6). The near-surface increase with depth of the nadir radiance, which was discussed in Section 11.2 in relation to Fig. 5.3, finally disappears at $f_s \approx 0.1$.

The top curve (at $\theta_v = 180°$) in Fig. 11.6 shows the radiance at $\zeta = 0$ for a cardioidal sky, which corresponds to a very heavy overcast with no discernable sun. Tyler (1960) also measured an underwater radiance distribution on such a day. Figure 11.7 shows his relative radiances at $z = 6.1$ m (diamonds) and at $z = 0.025$ m (dots). [The measurements at $z = 0.025$ m are not given in his data report of 1960; the values shown here were extracted by eye from the figure in Tyler (1958).] The solid lines show the model predictions at the same depths, normalized to one at $\theta_v = 0°$ and $z = 6.1$ m. The same IOP's were used in this simulation as were used for the clear-sky comparison of Fig. 11.3. (The data were taken six weeks apart, during which time the IOP's may have changed appreciably.) The numerical model is once again in good agreement with Tyler's

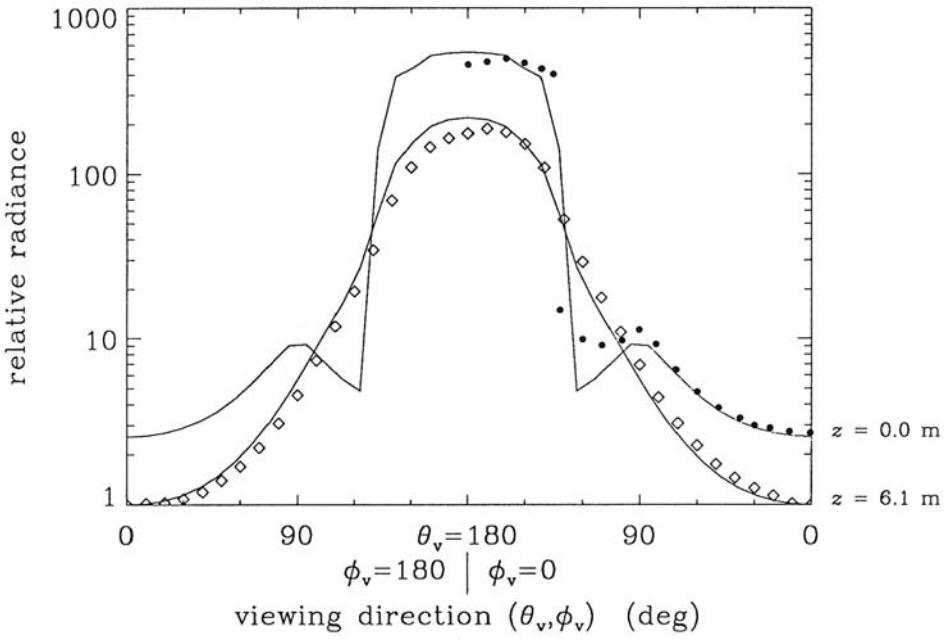

Fig. 11.7. Model-data comparison. The diamonds and dots are radiances measured by Tyler (1960 and 1958, respectively) for a heavily overcast sky; the solid lines are the corresponding model predictions.

measurements, considering the uncertainties in the assumptions made about the IOP's.

The four-order-of-magnitude radiance differences seen within the Snell circle at $\zeta = 0$ in Fig. 11.6 diminish with depth, as scattering redirects the photons and thereby destroys the information they carry about their original directions. Figure 11.8 shows the radiances at $\zeta = 5$. Now the radiances differ at most by an order of magnitude for a given θ_v. Note also that the profile corresponding to the overcast sky ($f_s = 1$) is already close to its asymptotic shape. We already have seen another manifestation of this behavior in the *K*-functions of Figs. 9.5(b) and 9.6(b).

Simulations such as we have just discussed give us great insight into the influence of sky conditions on underwater radiance distributions. However, for many purposes of optical oceanography, such radiance differences have relatively unimportant consequences. Note in Figs. 11.6 and 11.8 that the cardioidal sky ($f_s = 1$) often gives the highest radiance within the Snell circle, but the lowest radiance outside the circle; the converse is often true for the black sky case ($f_s = 0$). We thus anticipate

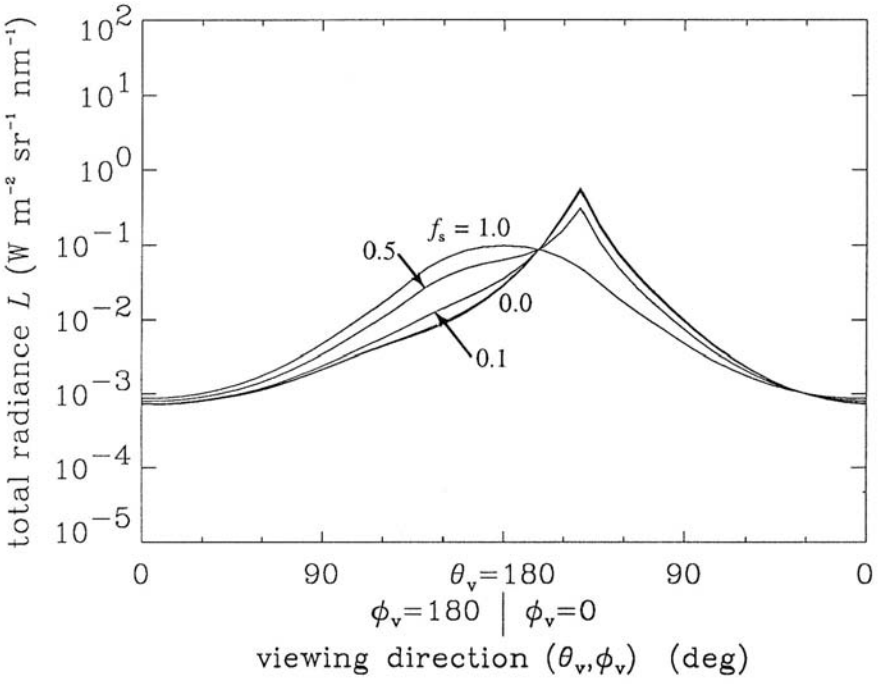

Fig. 11.8. Computed radiance profiles at five optical depths (ζ = 5) for different ratios f_s of sky to total incident irradiance, as in Fig. 11.6.

that when we compute a quantity such as E_o, the total scalar irradiance, the radiance differences will tend to cancel out. This is indeed the case.

Table 11.3 shows the effect of sky conditions on selected irradiances and apparent optical properties. When studying this table, remember that the total incident irradiance $E_{od}(a)$ is held constant; only the relative contributions of the diffuse sky and direct solar beam vary, as shown in Eq. (11.2). Remember also that we are presenting one set of simulations for a level water surface, $\omega_o = 0.8$, sun at 57°, etc. With these caveats in mind, we see that the values of E_d just below the surface have only a roughly 6% spread in values as we go from a black sky to a fully overcast sky. The associated K-function, K_d, varies by about 9%. When K_d is normalized by Gordon's method as described in Section 3.2, the normalized K_d's vary by only 2%. (For this normalization, the values of $E_d(\zeta=a)$, which are known in the numerical simulation, were used to approximate Gordon's f factor.) Thus the effect of sky conditions on K_d is largely removed by Gordon's normalization.

The effect of sky condition on the total scalar irradiance E_o is even less: 3% for E_o and 6% for K_o, just below the water surface. At one optical

Table 11.3. Selected irradiances and apparent optical properties as a function of sky condition f_s. These quantities are derived from the radiance distributions shown in Fig. 11.6. All quantities have appropriate units, and magnitudes relative to an incident total (sky + sun) irradiance of $E_{od}(a) = 1$ W m^{-2} nm^{-1}.

quantity (depth)	f_s					spread of values
	0.0	0.1	0.5	0.9	1.0	
$E_d(\zeta=w)$	0.528	0.532	0.544	0.557	0.560	~6%
$K_d(\zeta=w)$	0.287	0.285	0.275	0.266	0.263	~9%
$E_o(\zeta=w)$	0.743	0.741	0.734	0.726	0.724	~3%
$K_o(\zeta=w)$	0.188	0.187	0.183	0.178	0.177	~6%
$E_o(\zeta=1)$	0.587	0.586	0.584	0.583	0.583	~1%
$K_o(\zeta=1)$	0.267	0.267	0.254	0.244	0.242	~10%
$R_{rs}(\zeta=a)$	3.43−3[a]	3.53−3	3.50−3	3.48−3	3.46−3	~2%

a. 3.43−3 means 3.43×10^{-3}, etc.

depth, E_o values vary by less than 1%, although there is a 10% variation in K_o at $\zeta = 1$.

The remote-sensing reflectance $R_{rs}(\theta_v=0)$ varies by only 2%. Note that in computing R_{rs}, we have first removed the effect of the downwelling sky radiance that is reflected back upward by the water surface. If the total (water-leaving plus reflected) zenith radiance just above the surface were used in Eq. (10.24), then R_{rs} would increase by a factor of 3.5 in going from the black sky to the cardioidal sky. The correction for the surface-reflected sky radiance is trivial in the present instance, because the water surface is level. Nevertheless, this point illustrates the importance of being able to accurately compute the bidirectional reflectance properties of the sea surface when correcting remotely sensed radiances.

Tran and Collins (1990) used LOWTRAN-7 atmospheric radiative transfer calculations to show that f_s, averaged over all visible wavelengths, is typically in the range from 0.2 to 0.5 for clear sky conditions (horizontal visibility at sea level greater than ~20 km). Only for very hazy skies (visibility less than 5 km) does f_s reach 0.8. Thus, we can expect even less variability in nature than that shown in Table 11.3.

However, different atmospheric models can yield significantly different values of $E_{od}(a)$. The model comparison of Mobley, *et al.* (1993)

found an 18% spread in $E_d(a)$ values. Different E_d or E_{od} values in the air will affect the absolute values of irradiances within the water, but will not affect the AOP's, which do not depend on the magnitudes of the radiometric quantities.

11.4 Sea-surface Effects

The preceding simulations all have been for a level water surface. We next investigate the effects of a wind-blown surface on underwater light fields. We shall simulate the same basic water body as before: $\tilde{\beta} = \tilde{\beta}_p$, $\omega_o = 0.8$, sun at $\theta_s = 57°$, and so on. We shall take the ratio of sky-to-total incident irradiance to be $f_s = 0.3$, which is typical of natural conditions. Now, however, we shall let the water surface be covered by capillary waves. The waves, and their radiative transfer properties, are computed as described in Chapter 4.

Figure 11.9 shows the radiance distribution just beneath the water surface for wind speeds of $U = 0$, 5, and 10 m s^{-1}. The most noticeable effect of the increasing wind speed is to broaden the angular width of the sun's image as seen from below the surface. This phenomenon is well known to any scuba diver who has looked upward and observed the "glitter pattern" of the sun's rays coming through a wind-blown surface. A wind-blown surface also gives a reflected glitter pattern when the sea surface is viewed from above. The solid line in Fig. 11.10(a) shows the radiance distribution just *above* the water surface for the case of no wind. The dashed line is the radiance just *below* the surface, as is displayed in Fig. 11.9. For viewing angles $90° < \theta_v \le 180°$, we are seeing the downwelling cardioidal sky radiance except at $(\theta_v,\phi_v) = (123°,0°)$, in which case we are looking into the quad containing the sun. In viewing direction $(\theta_v,\phi_v) = (57°,0°)$ we are looking downward at the water surface and seeing the specular reflection of the sun in the level water surface. Note that the ratio of these radiances is $L^-(\theta_v = 57°)/L^+(\theta_v = 123°) \approx 1/21 \approx 0.05$, which equals the quad-averaged reflectance for the quad centered at $\theta = 57°$, as seen in Fig. 4.21. (The contribution of the water-leaving radiance to the plotted total radiance is quite small in the present case.)

Figure 11.10(b) shows the same situation when the surface is covered with capillary waves corresponding to a 5 m s^{-1} wind. The significant difference in these two figures is that the sun's specular reflection in the water surface for $U = 0$ is now spread out over a large angular glitter pattern ranging from the viewer's horizon almost to the nadir.

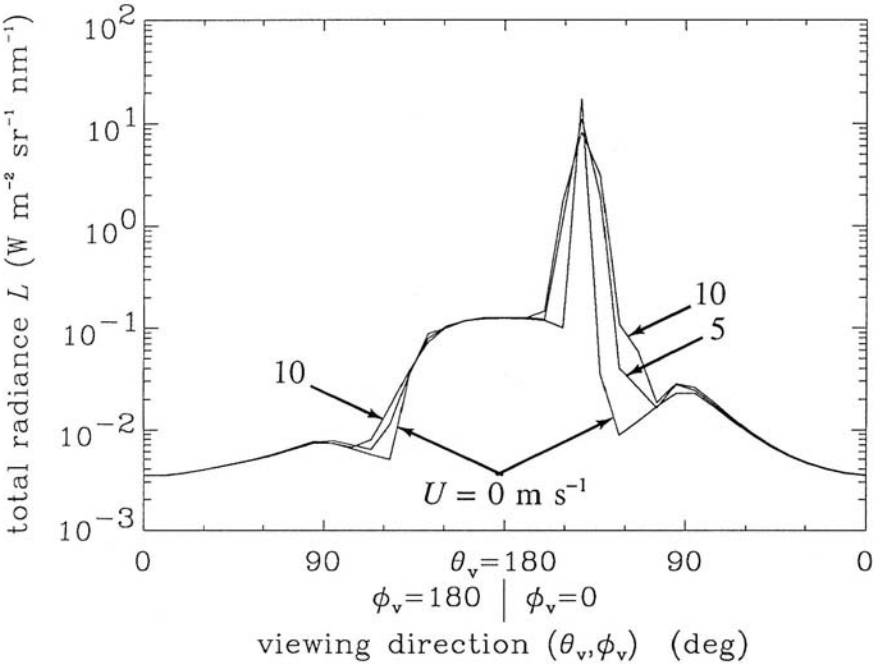

Fig. 11.9. Computed radiance distribuion in the plane of the sun and just below the surface, for wind speeds of U = 0, 5, and 10 m s^{-1}. The surface is covered by capillary waves.

Numerical simulations of such transmitted and reflected glitter patterns can be seen in Preisendorfer and Mobley (1986). In Figs. 11.9 and 11.10, we are seeing the physics of the glitter patterns expressed in terms of the time-averaged radiances.

The angular redistribution of the downwelling radiance by the capillary waves as seen in Fig. 11.9 has little effect on irradiances and AOP's. The spread of near-surface values of the irradiances, nadir and zenith radiances, and K-functions corresponding to Fig. 11.9 is at most a few percent. However, these simulations based on a surface covered by capillary waves do not entitle us to conclude that wave effects are unimportant for in-water optics. Reference to Figs. 4.11 or 4.12 shows that the surface irradiance reflectance $r(a,w)$ is relatively insensitive to wind speed for a solar angle of $\theta_s = 57°$. This is not the case at larger zenith angles or for overcast skies (Fig. 4.16); in such cases the capillary waves can significantly alter the amount of energy entering the water. But more importantly, the capillary-wave treatment of a wind-blown surface is inadequate at higher wind speeds (U greater than ~10 m s^{-1}).

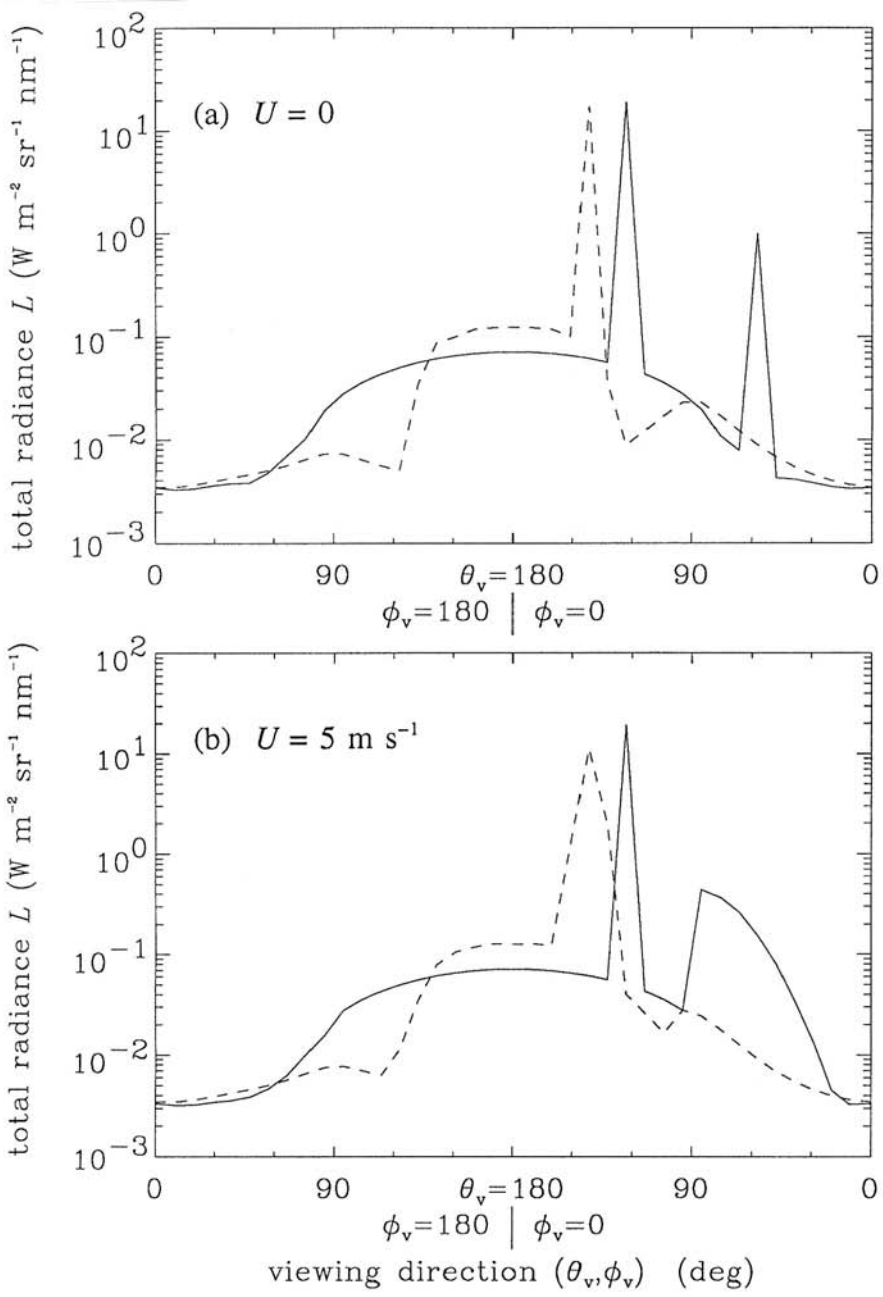

Fig. 11.10. Panel (a) shows the computed radiances just above (solid line) and just below (dashed line) the water surface, for the case of no wind; the surface is level. Panel (b) is the same situation for a 5 m s^{-1} wind; the surface is covered by capillary waves.

Figure 11.11 shows measured values of E_d, E_u and L_u at $\lambda = 410$ nm compared with model predictions. As usual, the IOP's were not measured in conjunction with the radiometric variables, so we had to make some educated guesses for modeling purposes. Water samples were taken at selected depths for chlorophyll analysis, so we used the average value of C in the bio-optical models of Eqs. (3.27) and (3.40) to estimate a and b. We then kept ω_o constant, and adjusted the values of a and b until the numerical results had the right depth dependence (K-functions). These adjustments were well within the ranges of variability of a and b seen in Figs. 3.7 and 3.20. The incident irradiance $E_{od}(a)$ was not measured, so we ran the model with $E_{od}(a) = 1$ W m^{-2} nm^{-1} and then scaled the output so that model and data agree at $z = 10$ m. The good agreement in the depth dependence of E_d at all depths and of E_u and L_u below 10 m indicates that we must have guessed reasonable values for a and b; the good agreement continues to the greatest depth of observation at $z = 50$ m. How then can the predicted values of E_u and L_u be so inaccurate in the upper few meters of water, even though the predicted E_d is quite satisfactory near the surface?

A plausible explanation of the discrepancies in E_u and L_u is as follows. These data were taken on a day when even the fish were seasick. There were sustained 25 knot winds, with gusts to 45 knots (16-24 m s^{-1}; measured at 3 m above sea level). The sea surface was very rough and covered with breaking waves. Breaking waves inject downward plumes of small bubbles into the water; excellent photographs of this process occurring in a laboratory tank can be seen in Lamarre and Melville (1992). These bubbles range in size from millimeters down to tens of micrometers. The size distribution of bubbles larger than ~50 μm is often well fit by the Junge size distribution of Eq. (3.23) with a slope parameter of $s = 4$. The number concentration of bubbles at the surface (bubbles per m^3) is a strong function of wind speed; the concentration decreases exponentially with depth. The review by Wu (1988) gives empirical models for the bubble size and depth distributions.

At the high wind speeds associated with Fig. 11.11, high concentrations of bubbles should be found in the upper few meters of water. These bubbles scatter light strongly in all directions – this scattering is the reason that the bubbles appear white and highly visible when you dive into your swimming pool. The radiance in the downwelling solar beam just below the sea surface will be scattered mostly into downward directions. This redirection of the downwelling radiance will have a minimal effect in E_d, just as was the case for Fig. 11.9. However, the backscatter by bubbles in much greater than the backscatter by the water and its biological constituents. Thus, there will be relatively much more light backscattered

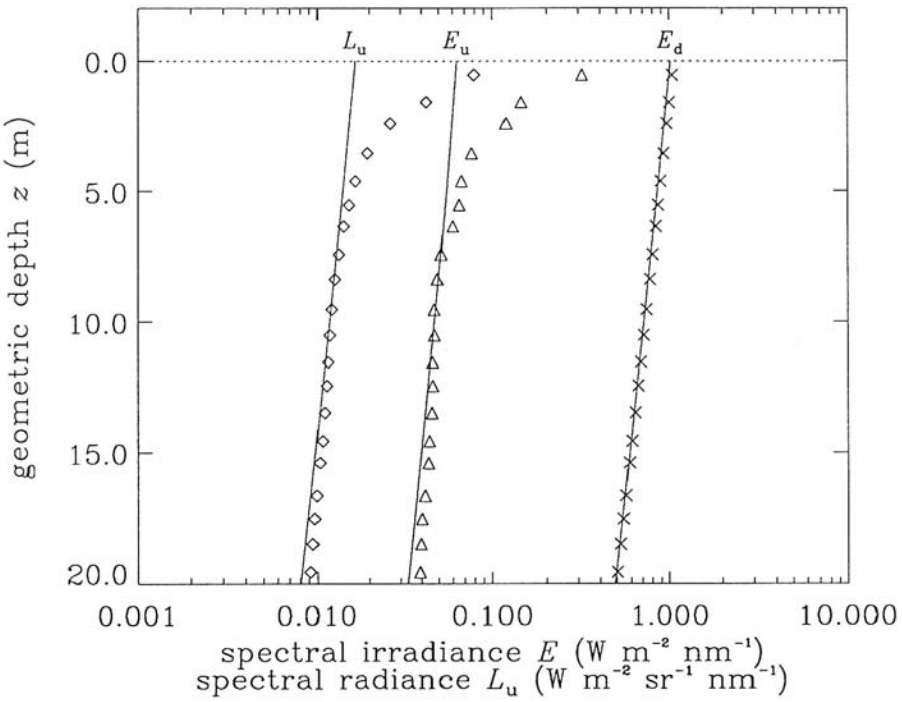

Fig. 11.11. Profiles of E_d, E_u, and L_u at $\lambda = 410$ nm measured under very rough sea-surface conditions. The near-surface behavior of E_u and L_u is believed to be due to bubbles. The solid lines give the normalized predictions of a model that does not include bubble effects. [data courtesy of C.O. Davis and W.J. Rhea]

by bubble-rich water than by bubble-free water. One view of a ship's wake verifies this statement. This backscattering by bubbles greatly increases E_u and L_u, as seen in Fig. 11.11. Simply stated, the nadir-viewing instruments "see" the bright bubbles against the dark water below; they therefore record large values for upwelling quantities. The zenith-viewing instruments see the bright bubbles against an already bright sky (as transmitted through the surface); they therefore record little change from the bubble-free case.

The effects of near-surface bubbles on acoustic scattering, and on gas and particle transport across the air-sea surface, have long been recognized. However, quantitative radiative transfer computations, as would be needed to model the data of Fig. 11.11 quantitatively, have not been made.

Figure 11.11 provides us with the perfect example of how a numerically sophisticated model, which solves its equations with high accuracy, nevertheless gives a grossly incorrect result because *the relevant*

physics was omitted from the model. In the present case, the omitted physics takes the form of the phase function and scattering coefficient that would be needed to describe the depth-dependent scattering effects of the bubbles.

We note also that the bubbles have little effect on the total in-water energy (expressed here with E_d as a proxy for E_o), because most of the energy is in the downwelling light field. The model without bubbles likely would be adequate for studies of plankton growth or water heating. On the other hand, the model without bubbles would be useless for remote sensing studies, because it underpredicts E_u and L_u by factors of five near the surface. Corresponding errors would appear in the water-leaving radiance or in $R(z{=}0)$.

This discussion also highlights how greatly oversimplified is the treatment of a wind-blown sea surface as being covered by capillary waves only. Bubbles within the water and foam on its surface can predominate in determining the radiative-transfer properties of the sea surface at higher wind speeds, yet these topics scarcely have been studied.

11.5 Bottom Effects

We next turn our attention to the effects of the bottom boundary. Once again, we simulate a water body with $\tilde{\beta} = \tilde{\beta}_p$, $\omega_o = 0.8$, the sun at $\theta_s = 57°$ contributing 0.7 of $E_{od}(a)$ and a cardioidal sky contributing 0.3 of $E_{od}(a)$.

The solid lines in Fig. 11.12 show the radiance distribution in the plane of the sun at $\zeta = 0$ and 5 optical depths, for the case of an infinitely deep water body. For this situation, the irradiance reflectance at $\zeta = 5$ is computed to be $R(5) \equiv E_u(5)/E_d(5) = 0.0384$. This is the reflectance $r(m,b) = r(5,\infty)$ of the infinitely thick slab of water $S[5,\infty]$. Now let us replace the infinitely deep slab of water $S[5,\infty]$ by an opaque Lambertian bottom $S[5,b]$ that has the same irradiance reflectance, namely $r(5,b) = 0.0384$, as the infinitely deep slab $S[5,\infty]$. The radiance distribution generated with this bottom boundary condition is shown by the dashed lines in Fig. 11.12. We see that the radiances are indistinguishable at $\zeta = 0$ and that the downwelling radiances are nearly identical at $\zeta = 5$. The upwelling radiances at $\zeta = 5$ are considerably different. Note in particular that the upwelling radiance just above the opaque bottom is isotropic, i.e., is constant for $0 \le \theta_v \le 90°$. This shows the effect of a Lambertian bottom on the reflected radiance, as was discussed in Section 4.11.

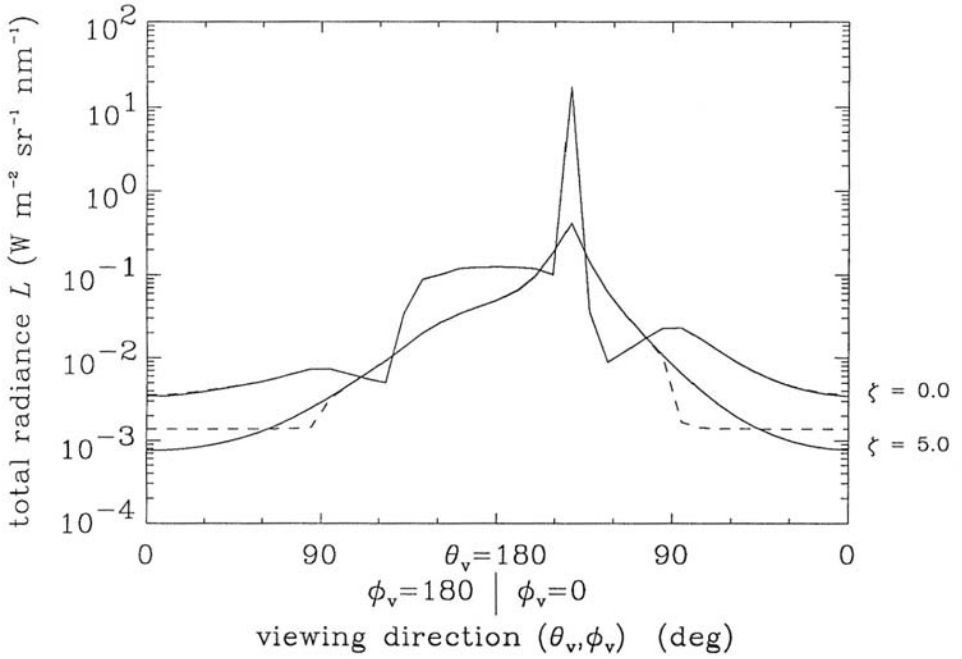

Fig. 11.12. Computed radiance distributions in the plane of the sun, just below the surface and at $\zeta = 5$ optical depths. The solid line is for an infinitely deep water body, and the dashed line is for a Lambertian bottom at $\zeta = 5$. The two bottom boundaries $S[5,\infty]$ and $S[5,b]$ have the same irradiance reflectance.

Figure 11.13 shows the irradiances and the zenith radiance L_u corresponding to Fig. 11.12. We see that the two different bottom types yield significantly different values for E_{ou} just above the bottom, and for L_u in the lower part of the water column. Note that the total nadir-viewing radiance, L_u(in air) in the figure, is almost the same for both bottoms. We now increase the reflectance of the Lambertian bottom to $r(5,b) = 0.5$. Such a boundary condition could represent a white sand bottom. Figure 11.14 shows the irradiances and zenith radiance for the infinitely-deep-water and white-sand cases. Now the highly reflecting bottom has greatly increased the upwelling light field both within the water and in the air just above the water. The nadir-viewing total radiance just above the surface has almost doubled [the plotted L_u(in air) includes both the true water-leaving radiance and diffuse sky light reflected by the surface, which is the same for both simulations]. We would have no trouble remotely sensing the presence of the sandy bottom.

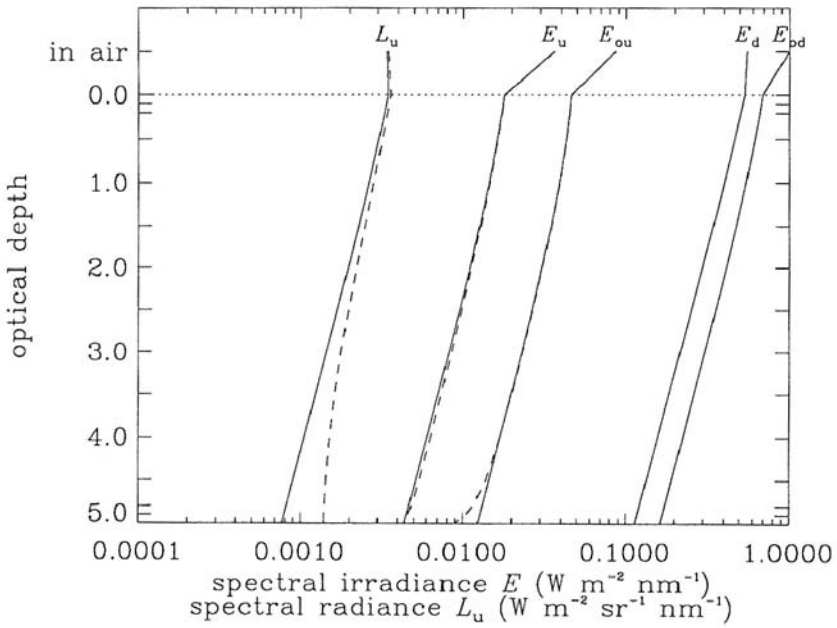

Fig. 11.13. Irradiances and zenith (nadir-viewing) radiance corresponding to Fig. 11.12. Both bottom boundaries have the same irradiance reflectance: $R(5) = r(5,b) = r(5,\infty) = 0.0384$.

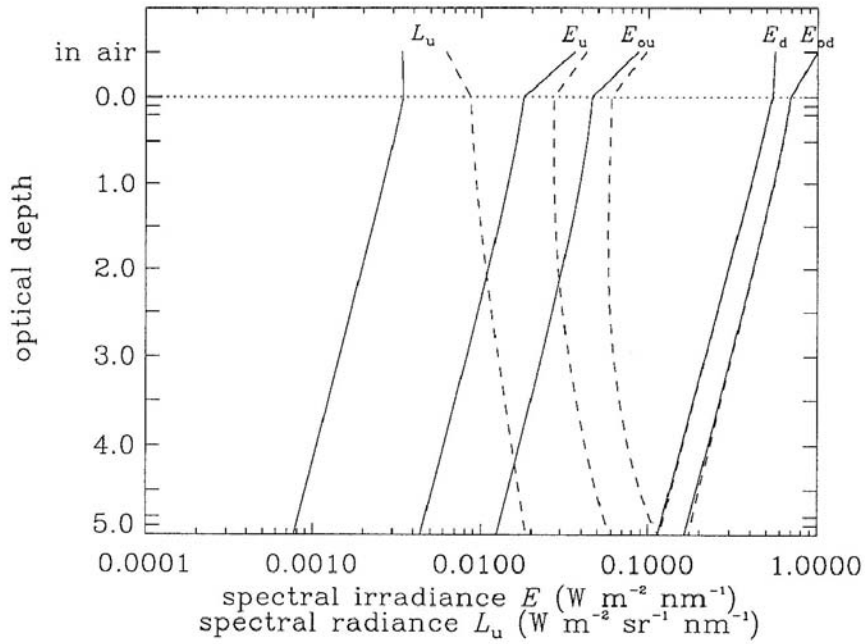

Fig. 11.14. Irradiances and zenith radiance for the infinitely deep water body of Figs. 11.12 and 11.13 (solid lines), and for a Lambertian bottom of reflectance $r(5,b) = 0.5$ (dashed lines).

Note from Fig. 11.14 that $E_{ou}(5) = E_d(5)$ for this case of a Lambertian bottom with $r(m,b) = 0.5$. We already encountered this result in problem 4.3. Note also that for the Lambertian bottom,

$$0.0186 = L_u(5) = \frac{r(5,b)}{\pi} E_d(5) = \frac{0.5}{\pi} 0.117 = 0.0186,$$

as is expected from Eq. (4.84). These two numerical checks are an indication that the numerical model is properly simulating a Lambertian bottom boundary.

11.6 Stratification Effects

For simplicity, the preceding simulations all have assumed the water to be homogenous. We now consider an idealized set of depth-dependent absorption and scattering coefficients, in order to illustrate the effects of changes in a and b with depth. Except for a and b, we keep things the same: sun at 57°, cardioidal sky contributing 30% of $E_{od}(a)$, $\tilde{\beta}_p$, level surface, etc.

Figure 11.15 is generated for infinitely deep water with "background" values of $a = b = 0.5$ m^{-1}. In Fig. 11.15(a), the absorption coefficient is increased to $a = 1.0$ m^{-1} between depths $\zeta = 10$ and $\zeta = 20$. Thus, $\omega_o = 0.333$ if $10 \le \zeta \le 20$, and $\omega_o = 0.5$ elsewhere. We note in Fig. 11.15(a) that the irradiances and L_u decrease more rapidly with optical depth within the highly absorbing layer than above or below it. The values of the nondimensional (i.e., derivatives taken with respect to optical depth) diffuse attenuation coefficients for E_d are

$$K_d^{nd}(5) = 0.661, \quad K_d^{nd}(15) = 0.786, \quad K_d^{nd}(25) = 0.603. \tag{11.3}$$

Likewise, we see in Fig. 11.15(b) that the light field decreases less rapidly with optical depth within the highly scattering layer. In this case,

$$K_d^{nd}(5) = 0.661, \quad K_d^{nd}(15) = 0.449, \quad K_d^{nd}(25) = 0.618. \tag{11.4}$$

Note that although the $K_d^{nd}(5)$ values are the same in the two simulations, the $K_d^{nd}(25)$ values differ, even though the IOP's of the lower layer are the same in each case. The reason for the difference is that the angular distribution of the radiance has been changed in a different way in passing through the highly absorbing layer than in passing through the highly scattering layer.

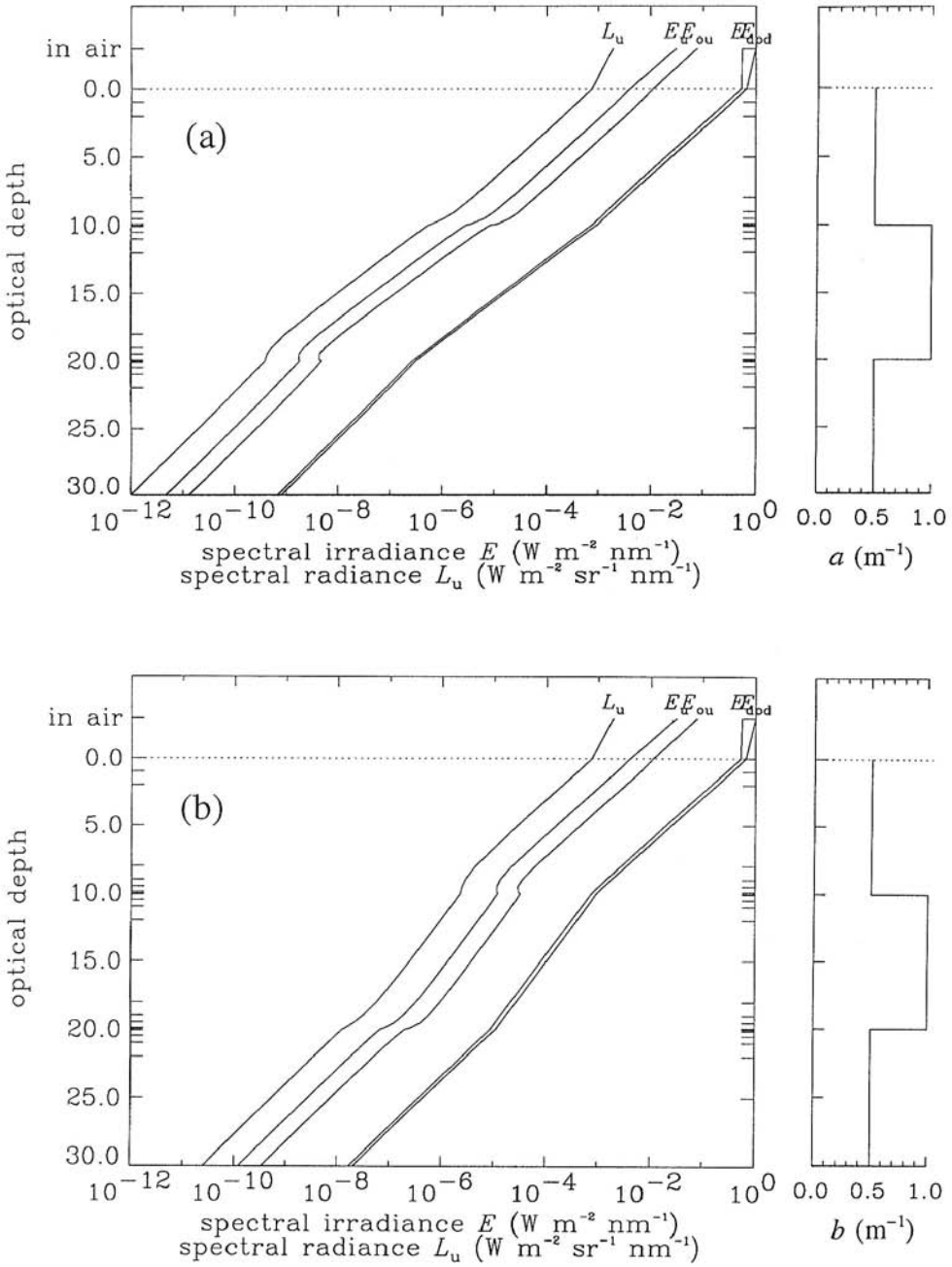

Fig. 11.15. Irradiances and zenith radiance for layered water bodies. In panel (a), the absorption coefficient a is increased by a factor of two between 10 and 20 optical depths; the scattering coefficient b is independent of depth. In panel (b), b is increased by a factor of two between $\zeta = 10$ and 20, and a is constant.

We also notice some interesting "fine structure" in the upwelling quantities near the discontinuities in a and b. Note, for example, how E_u and E_{ou} actually increase with optical depth just above the top of the highly scattering layer in Fig. 11.15(b), i.e., in the region from $\zeta = 9.5$ to 10.0. We are seeing here essentially the same physics as we saw in Fig. 11.14. In that figure, the highly reflective Lambertian bottom scattered more light upward than did the water itself, so that E_u, E_{ou} and L_u all increased with optical depth. In Fig. 11.15(b) near $\zeta = 10$, the highly scattering layer below $\zeta = 10$ is scattering so much light back into the region above $\zeta = 10$ that E_u and E_{ou} increase as the depth approaches $\zeta = 10$. The same phenomenon is seen in Fig. 11.15(a) just above $\zeta = 20$, where we once again go from a less-scattering to a more-scattering layer. The opposite effect occurs when we go from a more-scattering to a less-scattering layer, as in Fig. 11.15(a) near $\zeta = 10$ and in Fig. 11.15(b) near $\zeta = 20$. In these regions, less light is being scattered upward by the layer below, and E_u, E_{ou} and L_u decrease more rapidly with optical depth than they otherwise would.

Such behaviors seldom if ever would be observed in natural waters, because a and b do not change abruptly by factors of two. However, the presence of such effects in the simulations is a reassuring indication of the accuracy with which the numerical model is solving the RTE, even for discontinuous IOP's. It should be remembered that the Riccati equations of Chapter 8 are being integrated with arbitrarily fine depth resolution, even though we record the output only at preselected depths. Our invariant imbedding algorithm has *not* discretized the depth variable ζ (only the direction variable $\hat{\boldsymbol{\xi}}$).

11.7 Phase Function Effects

We now consider the consequences of changing the shape of the phase function $\tilde{\beta}$ while holding all else constant. Let us take $\omega_o = 0.2$. Table 3.5 shows that such a value is found in the clearest waters at blue wavelengths. Such a low value of ω_o also can occur in turbid waters at red wavelengths, where the high absorption by water itself dominates scattering.

The solid lines in Fig. 11.16 show the radiance as computed using the average particle phase function $\tilde{\beta}_p$ of Table 3.10. The dashed lines show the corresponding calculation made using the phase function for pure water, $\tilde{\beta}_w$, as given by Eq. (3.30).

Just below the surface, the downwelling radiances within the Snell circle are nearly equal. Outside the Snell circle, however, the radiance computed with $\tilde{\beta}_w$ is as much as 36 times greater than that for $\tilde{\beta}_p$. This

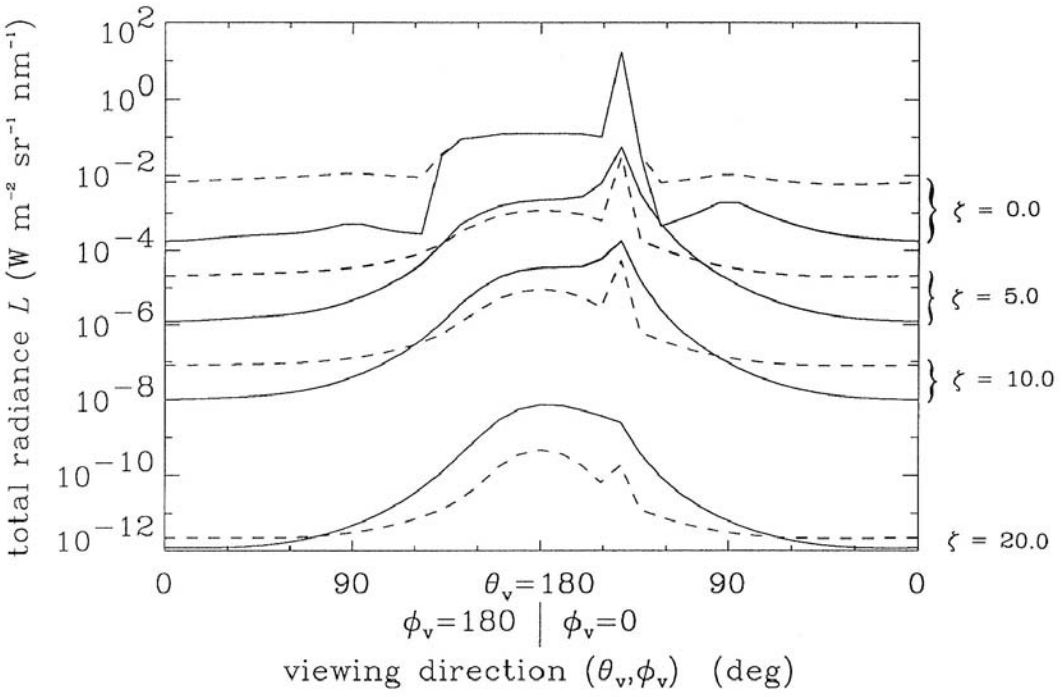

Fig. 11.16. Radiance distributions in the plane of the sun's rays for the average particle phase function $\tilde{\beta}_p$ (solid lines) and for a pure-water phase function $\tilde{\beta}_w$ (dashed lines). Both instances have $\omega_o = 0.2$.

roughly stated inequality holds for all depths: downwelling radiances are greater for $\tilde{\beta}_p$ and upwelling radiances are greater for $\tilde{\beta}_w$. This behavior is a straightforward consequence of the ratios of forward to backward scattering for the two phase functions. For $\tilde{\beta}_p$, the incident downwelling photons tend to keep heading downward even as they are multiply scattered. For $\tilde{\beta}_w$, even single scattering redirects many photons into upward directions. The radiance distribution for $\tilde{\beta}_w$ therefore becomes much more uniform than the one for $\tilde{\beta}_p$. The radiance distribution of course never becomes isotropic, even for an isotropic $\tilde{\beta}$; recall Eq. (9.88).

The irradiances and zenith radiance corresponding to Fig. 11.16 are seen in Fig. 11.17. As expected, the downwelling irradiances E_d and E_{od} are greater for $\tilde{\beta}_p$ (solid lines), and the upwelling quantities E_u, E_{ou}, and L_u are greater for $\tilde{\beta}_w$ (dashed lines).

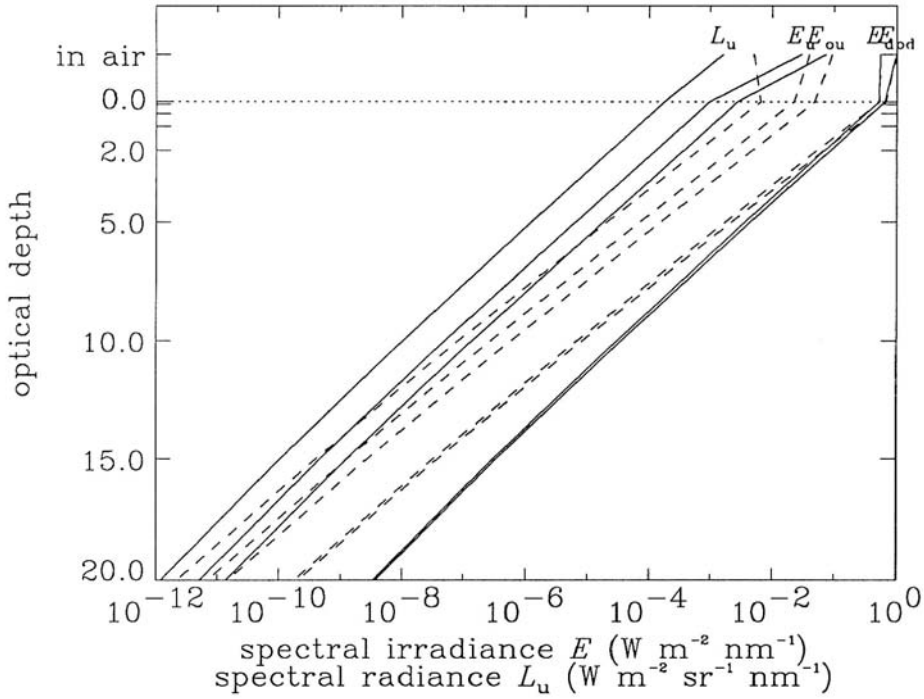

Fig. 11.17. Irradiances and zenith radiance corresponding to Fig. 11.16.

11.8 A Simulation of Case 1 Water

We now finish our book with one grand simulation of the light field as might be observed at a particular moment at a particular location at sea. As above, we are more interested in illustrating the modeling process and in building our intuition than in solving a specific problem. In any case, we have no measurements for comparison with our predictions. Nevertheless, a comprehensive simulation can be very educational when viewed as an experiment under our complete control. If nothing else, we shall remind ourselves of the vast quantity of information that can be extracted from a computed or measured spectral radiance distribution.

Wavelength discretization

We must compute the radiance over the entire visible spectrum in order to compute PAR, water heating, water color, or other quantities that depend on the net effect of light at those wavelengths present in natural

waters. Recall that the directionally (quad-) averaged RTE (8.7) is still a continuous function of wavelength. We must therefore now discretize our equations in the wavelength variable, so that we have only a finite number of equations to solve. This discretization can be effected in a rigorous fashion by integrating the RTE over a finite number N_λ of wavelength bands $\Delta\lambda_i$ and defining, for example,

$$L(\lambda_i) \equiv \frac{1}{\Delta\lambda_i} \int_{\Delta\lambda_i} L(\lambda)\, d\lambda \ , \ i = 1, 2, ..., N_\lambda \, .$$

Indeed, a mathematical formalism for wavelength discretization can be set up in a manner exactly analogous to the quad-averaging formalism. We shall forego this pleasure here; the details can be seen in Preisendorfer and Mobley (1988). In such a wavelength discretization, the RTE (5.20) becomes a matrix equation with, for example, the (i,j) element of the scattering term describing how radiance $L(\lambda_i)$ is scattered into $L(\lambda_j)$ – elastically if $i = j$ and inelastically if $i \neq j$. For our present purposes, it suffices simply to think of replacing λ by λ_i throughout the RTE and then regarding all wavelength-dependent values as being averages over some small wavelength interval $\Delta\lambda_i$.

For the present simulation, we choose the set of discrete wavelengths λ_i, $i = 1, 2, ..., N_\lambda \equiv 31$, to be $\lambda_1 = 400$ nm, 410, ..., 690, 700 nm $= \lambda_{31}$. Each $\Delta\lambda_i$ has the same value: $\Delta\lambda = 10$ nm.

The inherent optical properties of the water will be wavelength dependent, which means that the correspondence between optical depth and geometric depth will depend on wavelength. Although the numerical model solves the RTE in terms of optical depth at each particular wavelength, we can require it to give us output at those optical depths (different for each wavelength) that correspond to a preselected set of geometric depths. We can then analyze the model output in terms of geometric depth. For example, we can plot irradiances as functions of geometric depth and wavelength, as is customary in optical oceanography and limnology.

We keep other computational details the same as before. For example, we again use the equal $\Delta\theta$ quad partition of Fig. 4.19(b), which has 10 θ-bands and 24 ϕ-bands in each hemisphere of Ξ.

Inherent optical properties and boundary conditions

We begin our simulation by choosing a depth profile of chlorophyll and assuming that the water body is "average" case 1 water. Chlorophyll profiles are often well approximated as a background value plus a Gaussian

[Lewis, *et al*. (1983); recall Fig. 3.22]:

$$C(z) = C_o + \frac{h}{s\sqrt{2\pi}} \exp\left[-\frac{1}{2}\left(\frac{z - z_{max}}{s}\right)^2\right]. \tag{11.5}$$

The parameters C_o, h, s, and z_{max} vary greatly with time and location. Platt and Sathyendranath (1988) show that Eq. (11.5) with the parameter values

$$\begin{aligned} C_o &= 0.2 \text{ mg m}^{-3} \\ h &= 144 \text{ mg m}^{-2} \\ s &= 9 \text{ m} \\ z_{max} &= 17 \text{ m} \end{aligned} \tag{11.6}$$

gives a good fit to measured $C(z)$ values in the Celtic Sea in May. We therefore adopt Eqs. (11.5) and (11.6) for our simulation. Figure 11.18 shows the resulting $C(z)$ profile. Note that $C(z)$ reaches its maximum at $z = 17$ m.

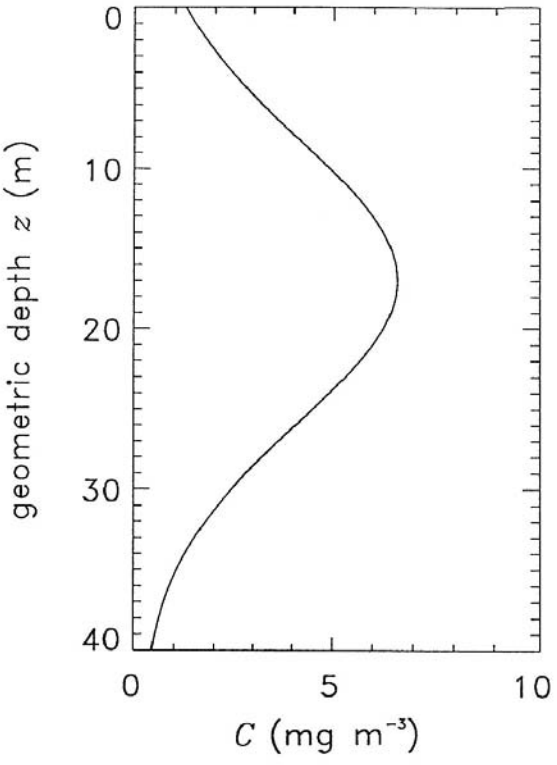

Fig. 11.18. Chlorophyll concentration $C(z)$ given by Eqs. (11.5) and (11.6).

The parameter values of Eq. (11.6) yield fairly high chlorophyll values, as are appropriate to the "green" coastal waters of the Celtic Sea. Nevertheless, we can model these waters as case 1 water, if we assume that the chlorophyll-bearing phytoplankton and their covarying by-products are dominant in determining the inherent optical properties of the water. The bio-optical models of Chapter 3 then give us the wavelength- and depth-dependent absorption and scattering coefficients, and related quantities.

The total absorption coefficient $a(z;\lambda)$ is obtained from Eq. (3.27) upon substitution of the assumed $C(z)$ profile. Figure 11.19 shows the resulting $a(z;\lambda)$. Panel (a) shows $a(z;\lambda)$ as a function of depth for selected wavelengths; panel b shows $a(z;\lambda)$ as a function of wavelength for selected depths. The maximum in a at $z = 17$ m reflects the contribution to absorption by phytoplankton pigments and associated detritus and yellow matter. The large values of a at $\lambda > 600$ nm are a consequence of absorption by the water itself.

The total scattering coefficient $b(z;\lambda)$ is obtained from $C(z)$ and the bio-optical model of Eq. (3.40). Figure 11.20 shows $b(z;\lambda)$ for the same z and λ values used in Fig. 11.19. The strong influence of scattering by particles is apparent in panel (a); the assumed λ^{-1} wavelength dependence of b is obvious in panel (b).

Because $b(z;\lambda)$ is considerably larger in magnitude than is $a(z;\lambda)$, except at red wavelengths, the beam attenuation coefficient $c(z;\lambda) = a(z;\lambda) + b(z;\lambda)$ has a depth dependence that is similar in appearance to the $b(z;\lambda)$ curves seen in Fig. 11.20(a). The high scattering at blue wavelengths and the high absorption at red wavelengths conspire to give $c(z;\lambda)$ values that do not vary greatly with wavelength. The $c(z;\lambda)$ behavior is shown in Fig. 11.21. Because the depth-averaged c value is of order 1 m^{-1} for all wavelengths, we see that a geometric depth of $z = 40$ m will correspond to roughly 40 optical depths at all wavelengths. Therefore, a computation of the light field to $z = 40$ m will be far deeper than would be necessary in studies of photosynthesis or remote sensing.

The $a(z;\lambda)$ and $b(z;\lambda)$ give an albedo of single scattering $\omega_o(z;\lambda)$ as seen in Fig. 11.22. Note that ω_o ranges from less than 0.2 to almost 0.9, depending on wavelength and depth. Thus, depending on the wavelength, the same water body can be highly absorbing, highly scattering, or anything in between.

The phase function is modelled using Eq. (3.13) with two terms:

$$\tilde{\beta}(z;\psi;\lambda) = \frac{b_w(\lambda)}{b(z;\lambda)}\tilde{\beta}_w(\psi) + \frac{b_p(z;\lambda)}{b(z;\lambda)}\tilde{\beta}_p(\psi) .$$

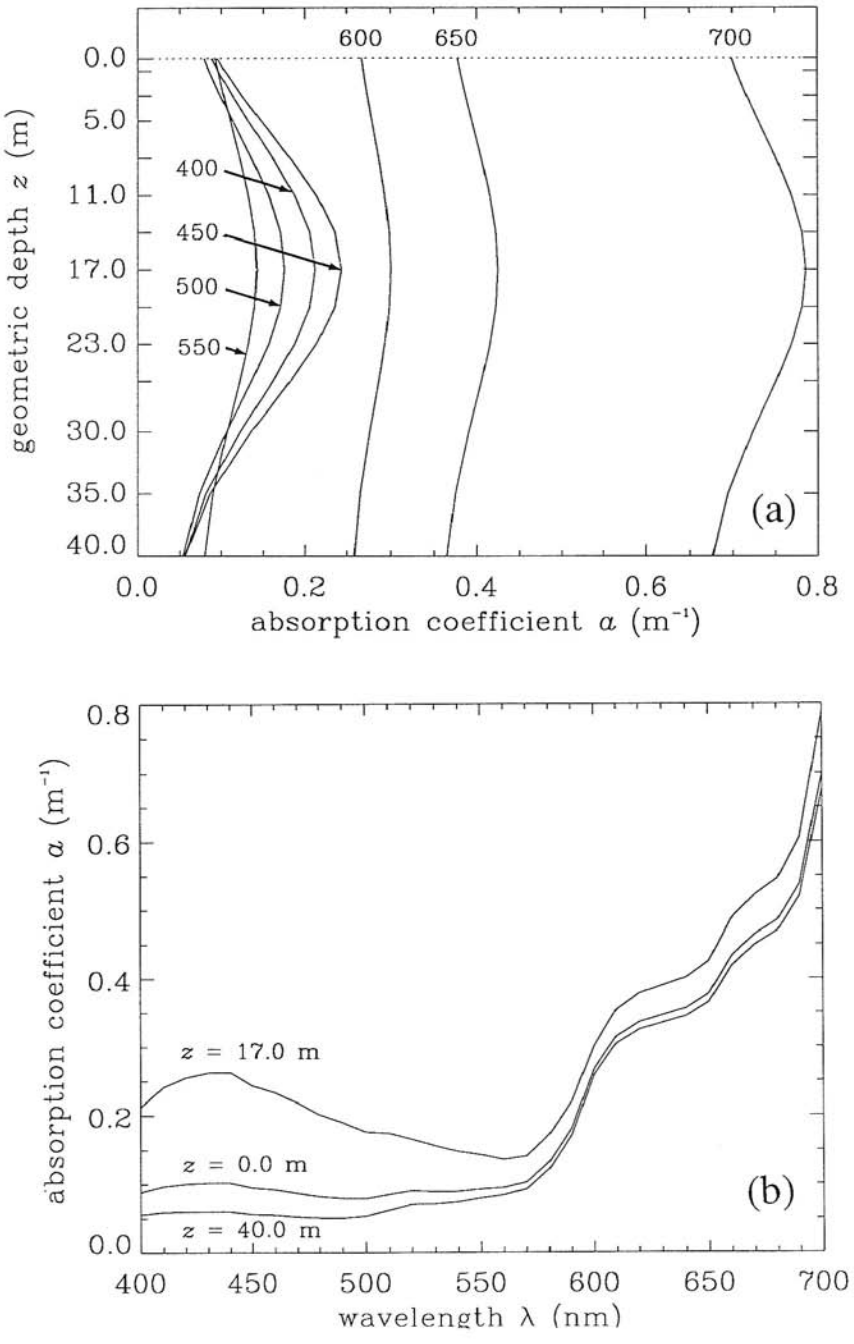

Fig. 11.19. The total absorption coefficient $a(z;\lambda)$ at selected depths and wavelengths, as used in the simulation. Panel (a) gives $a(z;\lambda)$ at 50 nm intervals from $\lambda = 400$ nm to $\lambda = 700$ nm. Panel (b) shows $a(z;\lambda)$ at three selected depths.

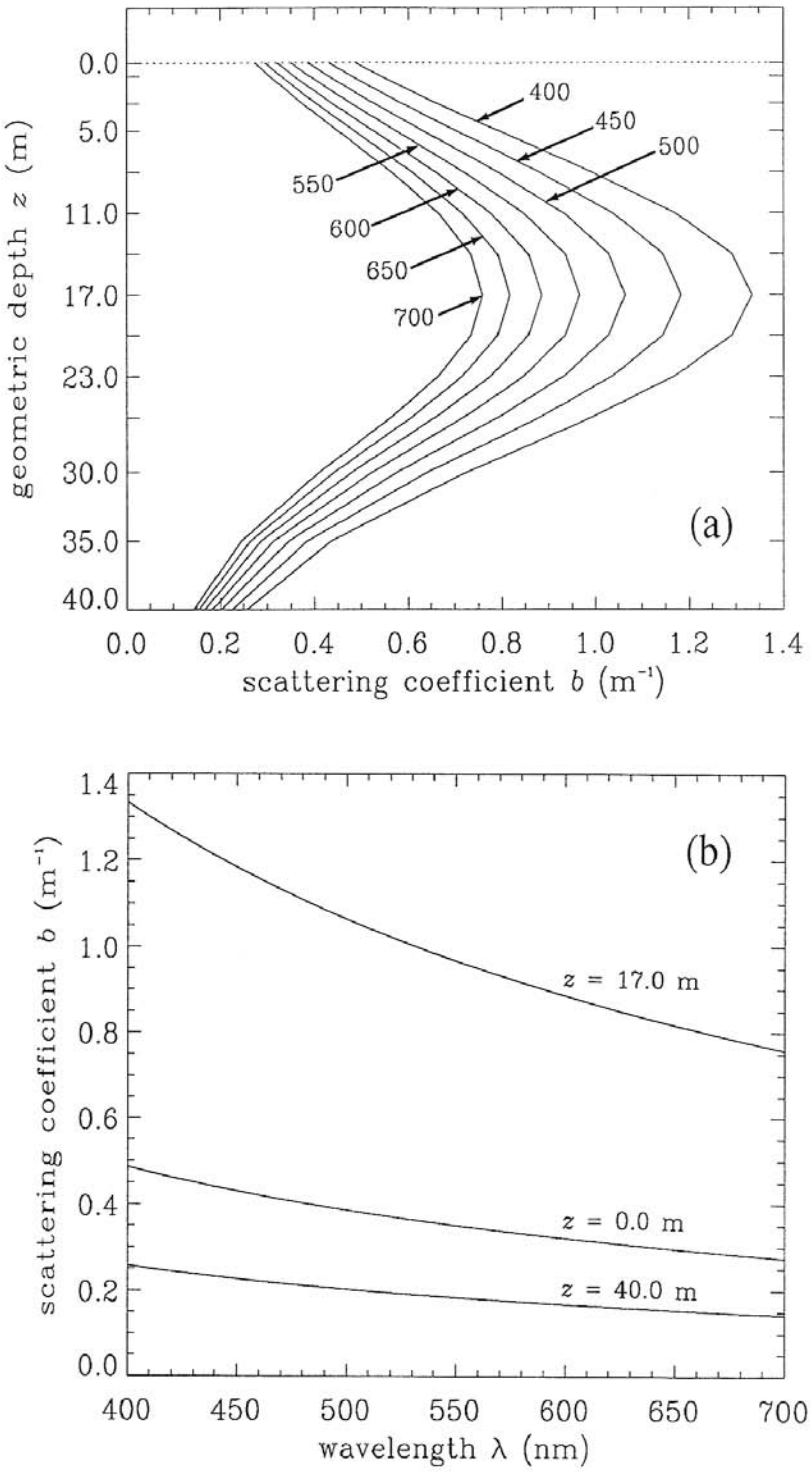

Fig. 11.20. The total scattering coefficient $b(z;\lambda)$ at selected depths and wavelengths. The format is the same as in Fig. 11.19.

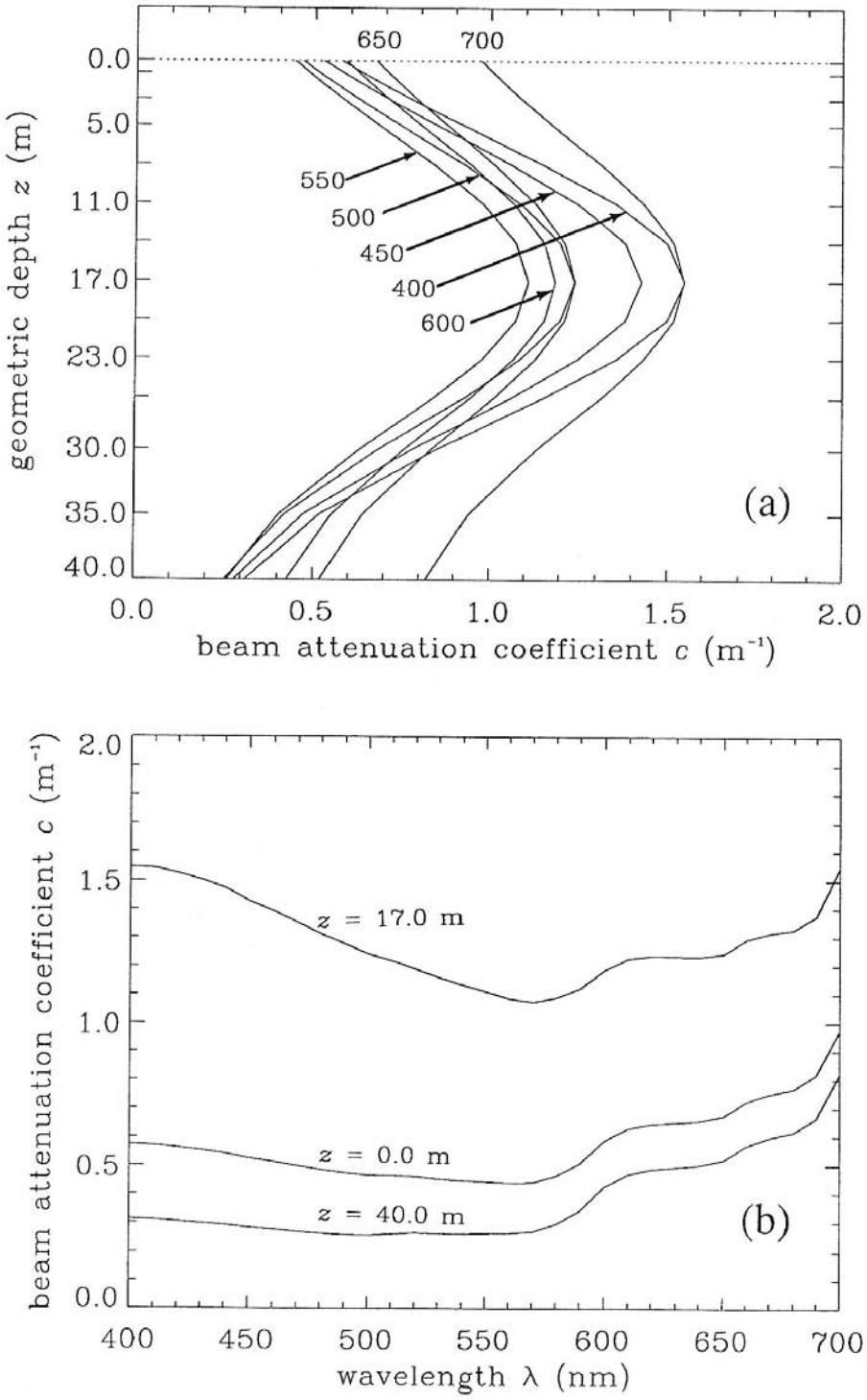

Fig. 11.21. The beam attenuation coefficient $c(z;\lambda)$ at selected depths and wavelengths. The format is the same as in Fig. 11.19.

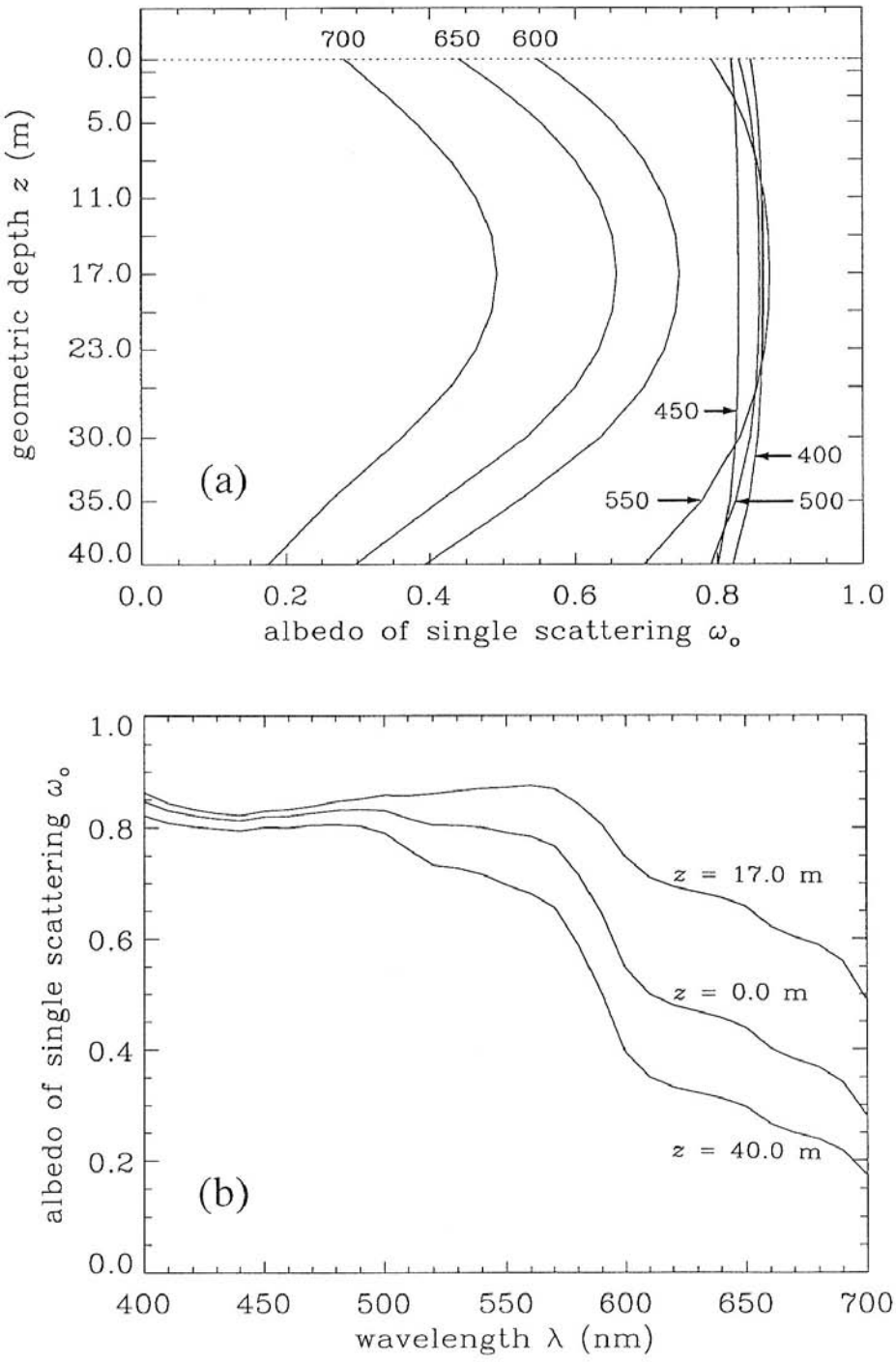

Fig. 11.22. The albedo of single scattering $\omega_o(z;\lambda)$ at selected depths and wavelengths. The format is the same as in Fig. 11.19.

Here $b_w(\lambda)$ is the depth-independent scattering coefficient for pure sea water; its value given by the Smith and Baker data of Table 3.5. The pure-water phase function $\tilde{\beta}_w(\psi)$ is given by Eq. (3.30). The particle scattering coefficient $b_p(z;\lambda)$ is given by $b_p(z;\lambda) = b(z;\lambda) - b_w(\lambda)$, where $b(z;\lambda)$ is obtained from Eq. (3.40) as described above. The associated phase function $\tilde{\beta}_p(\psi)$ is taken to be the average particle phase function of Table 3.10. Because the scattering coefficients depend on depth and wavelength, so does the total phase function $\tilde{\beta}$. Figure 11.23 shows $\tilde{\beta}(z;\psi;\lambda)$ for three depths at λ = 500 nm. There is a 40% spread in $\tilde{\beta}(z;\psi;500)$ values for $\psi > 120°$. This variation results from the differing contributions of pure sea water, with its high backscattering, and particles. Note that the backscattering is highest at $z = 40$ m, where the chlorophyll concentration is the lowest. For forward scattering angles $\psi < 60°$, $\tilde{\beta}(z;\psi;\lambda)$ is indistinguishable from $\tilde{\beta}_p(\psi)$ as seen in Fig. 3.10.

The phase function at a given depth z shows a similar spread of values for different wavelengths. The spread is largest at $z = 40$ m, where pure water [whose scattering depends strongly on wavelength; recall Eq.

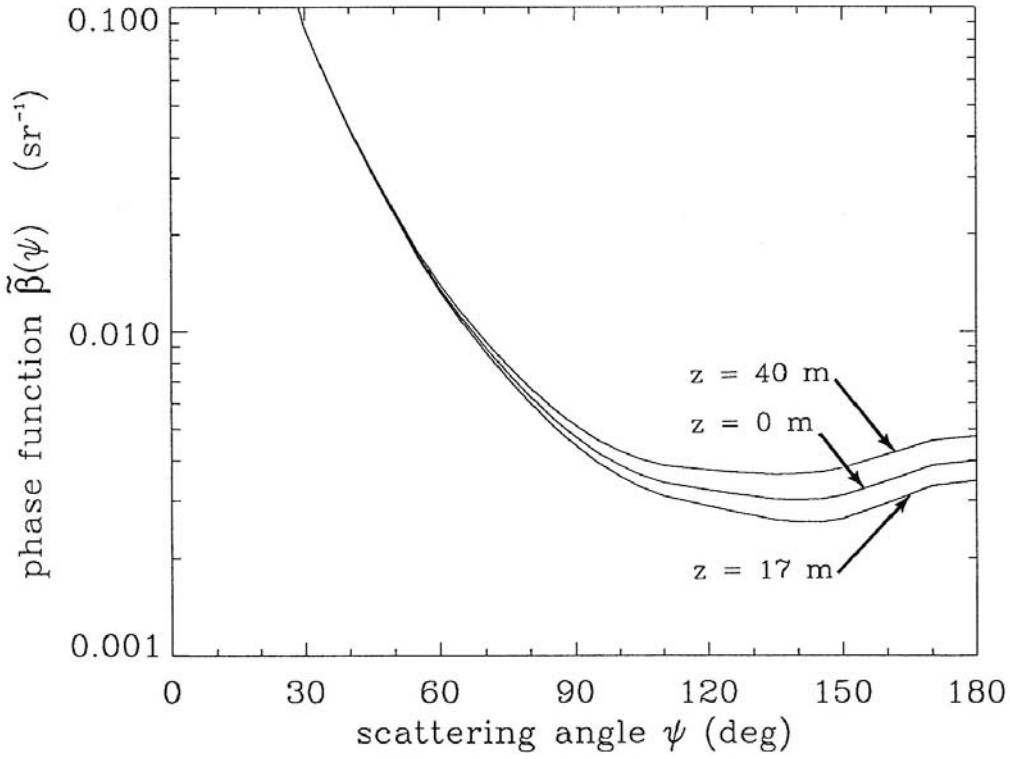

Fig. 11.23. The total phase function $\tilde{\beta}(z;\psi;\lambda)$ for three selected depths z and for λ = 500 nm.

(3.28)] makes the largest relative contribution to the total $\tilde{\beta}$. At z = 17 m, particle scattering [which depends only weakly on wavelength, recall Eq. (3.40)] dominates, and $\tilde{\beta}$ shows less dependence on λ. For a given depth, the backscattering is highest for λ = 400 nm and lowest for λ = 700 nm. We do not show the wavelength dependence of $\tilde{\beta}$, because the curves are very similar in appearance to those of Fig. 11.23.

We now have in hand the IOP's $\omega_o(z;\lambda)$ and $\tilde{\beta}(z;\psi;\lambda)$ needed to solve the RTE. We also have $c(z;\lambda)$, so that we can convert between optical and geometric depths. Note that the IOP's are given in terms of z, the numerical model solves the RTE (5.24) in terms of ζ, and the output is given in terms of z.

We shall omit chlorophyll fluorescence and other transpectral effects from our simulation for the simple reason that the associated terms, so laboriously developed in Chapter 5, have not yet been inserted into the author's computer code. If fluorescence were being included – as it should be in this high-chlorophyll water – the chlorophyll profile $C(z)$ would give us the information needed to start the fluorescence computations, beginning with Eq. (5.97).

It remains only to specify the boundary conditions. As before in this chapter, we place the sun in the quad centered at $(\theta_v,\phi_v) = (123°,0°)$. Thus, the sun's incoming rays are parallel to the wind direction. We let the solar direct beam contribute 70% of $E_{od}(a;\lambda)$, and a cardioidal distribution of diffuse sky radiance contributes the remaining 30% of $E_{od}(a;\lambda)$, at each wavelength. In our previous simulations in this chapter, which were all at one unspecified wavelength, it was permissible to set $E_{od}(a)$ = 1 W m^{-2} nm^{-1}. Now, however, we must use an actual solar spectrum to determine the value of $E_{od}(a;\lambda)$ at each wavelength, in order to properly reproduce the different amounts of irradiance incident at each wavelength. We use curve (c) of Fig. 1.2 for this purpose, even though that figure gives only the part of E_{od} due to the sun's direct beam, not the total E_{od}.

We model the water surface $S[a,w]$ as being covered with capillary waves corresponding to a wind speed of U = 5 m s^{-1}, as described in Chapter 4. The bottom boundary $S[z,b]$ is taken to be an infinitely deep, homogeneous body of water below the depth of greatest interest, z = 40 m. The IOP's of $S[z,b] = S[40\text{ m},\infty]$ are taken equal to their respective values at z = 40 m. The bidirectional radiance reflectance of $S[40,\infty]$ is computed as described in Chapter 9; recall in particular Eq. (9.76).

Radiances

The radiance distributions at the various wavelengths display in combination the features already seen in isolation in the preceding sections. Figure 11.24 shows the radiance at $\lambda = 400$ nm. Panel (a) is a cross-section of $L(z;\theta_v,\phi_v;\lambda=400)$ in the plane of the sun's incident rays; panel (b) is a cross-section perpendicular to the sun's rays. The dotted line gives the radiance in the air just above the water surface; solid lines are in the water. The magnitude of these radiances is determined by the value of $E_{od}(a;\lambda=400) = 0.354$ W m^{-2} nm^{-1}, as obtained from Fig. 1.2(c).

We note, for example, that the dotted line in Fig. 11.24(a) shows the glitter-pattern effect seen in Fig. 11.10(b). The underwater radiance at $z = 0.0$ shows the angular broadening of the sun's transmitted rays, as was seen in Fig. 11.9 for $U = 5$ m s^{-1}. The water is highly scattering at λ=400 nm: recall from Fig. 11.22 that $\omega_o(z;400) > 0.8$ for all z. We thus expect that the radiance at 400 nm should rapidly approach its asymptotic distribution, as it did for the ω_o =0.8 simulation seen in Fig. 11.5(a). This is precisely what happens. The radiance is visually almost indistinguishable from $L_\infty(\theta_v;400)$ at z = 17 m, which corresponds to $\zeta = 19.5$ at 400 nm.

The radiance at λ = 700 nm, where ω_o ranges from ~0.2 to ~0.5 depending on the depth, approaches $L_\infty(\theta_v;700)$ more slowly with depth. This is as we would expect from our discussion of the $\omega_o = 0.2$ simulation of Fig. 11.5(b). At λ = 700 nm, z = 40 m corresponds to $\zeta = 49.9$.

We shall not discuss the radiance distribution in any more detail, as we are now familiar with its general behavior.

Irradiances and K-functions

The spectral downwelling and upwelling plane irradiances $\boldsymbol{E_d(z;\lambda)}$ and $\boldsymbol{E_u(z;\lambda)}$ are the radiometric quantities most often measured in the field. Figure 11.25 shows these quantities at selected depths for the present simulation. The qualitative shapes of these E_d and E_u curves are very similar to what is seen in nature. Examples of irradiances measured in a variety of waters are seen, for example, in Tyler and Smith (1970) and, most recently, in Kishino (1994; his Fig. 4-3).

There are two features of our computed irradiances that differ from what is often measured in natural waters. First, our irradiances at depth increase with decreasing wavelength below 430 nm. This is a consequence of the decrease in $a(z;\lambda)$ for $\lambda < 430$ nm, as is seen in Fig. 11.19(b). Measured irradiances often tend to decrease below 430 nm. This is because the absorption often continues to increase with decreasing wavelength below

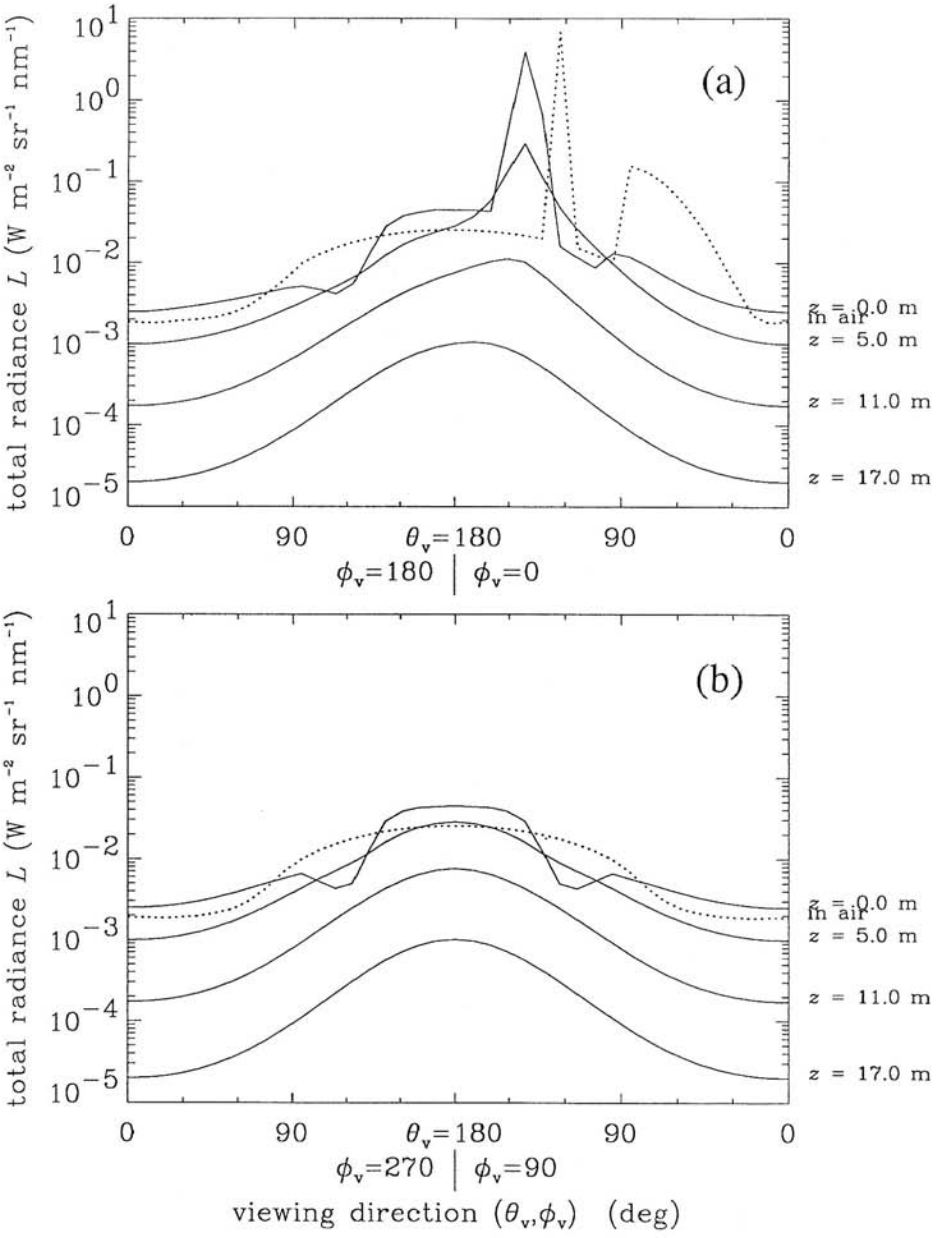

Fig. 11.24. The radiance distribution at λ = 400 nm in the plane of the sun's rays (panel a) and in the plane perpendicualr to the sun's rays (panel b). The dotted line is the radiance in the air, just above the water surface.

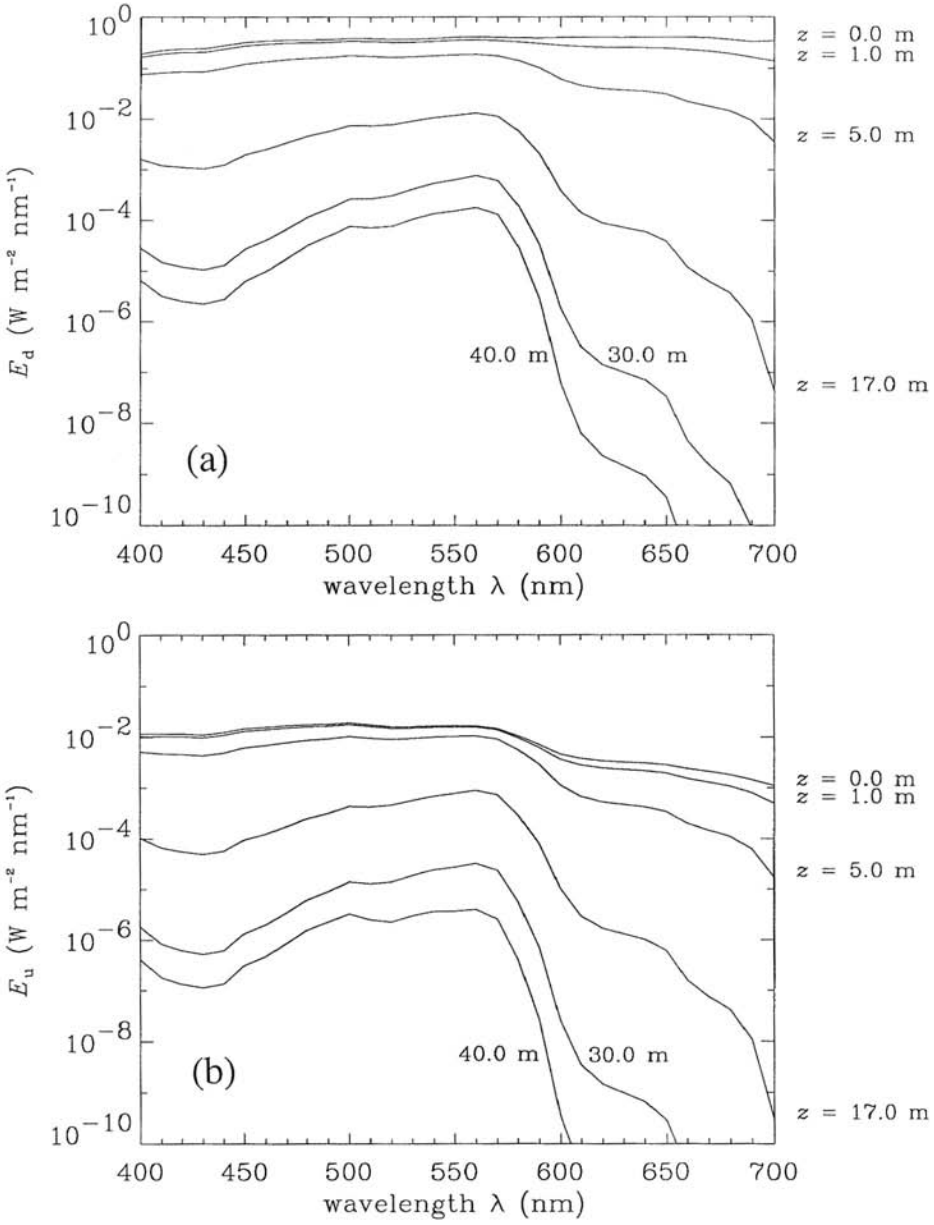

Fig. 11.25. Spectral downward (panel a) and upward (panel b) plane irradiances at selected depths.

430 nm; recall Figs. 3.9(b) and 3.9(c). This increase is a is most often due to the presence of yellow matter or other substances in the water. We have omitted any such substances in our model of $a(z;\lambda)$.

The second wavelength region in which our computations may differ from measurement is ~670 to ~700 nm, the wavelength band where chlorophyll fluorescence is strongest. There is often a pronounced "bump" in irradiance measurements near 685 nm; see for example Kishino (1994; especially his Fig. 4-3c, which shows measurements from the chlorophyll-rich waters of Tokyo Bay, Japan). Because the numerical model used in this simulation does not include fluorescence, we should be leery of its predictions in the chlorophyll emission band.

The depth–wavelength pattern of the total scalar irradiance $E_o(z;\lambda)$ is very similar to that seen for $E_d(z;\lambda)$ in Fig. 11.25(a), although the magnitude of E_o is always somewhat larger than E_d for a given z and λ.

Figure 11.26 shows $E_o(z;\lambda)$ as a function of depth for selected wavelengths. Note that the depth where E_o falls to 1% of its surface value varies from over 20 m at green wavelengths to about 5 m at red wavelengths. The diffuse attenuation coefficients $K_o(z;\lambda)$ associated with $E_o(z;\lambda)$ are shown in Fig. 11.27. These curves are similar in form and magnitude to the absorption curves seen in Fig. 11.19(a). This is just as we expect, because diffuse attenuation is largely determined by absorption; recall the discussions of Sections 5.12 and 10.4. Although those results pertained to K_d, the behavior of K_o seen here is similar to that of K_d.

The asymptotic values of the diffuse attenuation coefficients, $k_\infty(\lambda)$, vary from a minimum of 0.0802 m^{-1} at $\lambda = 490$ nm to a maximum of 0.7273 m^{-1} at $\lambda = 700$ nm.

The photosynthetically available radiation (PAR) is computed at each depth by Eq. (1.34). As a consequence of our chosen wavelength discretization, we can approximate Eq. (1.34) by

$$\mathrm{PAR}(z) \approx \frac{\Delta\lambda}{hc} \sum_{i=1}^{31} \lambda_i E_o(z;\lambda_i),$$

where, as previously noted, $\lambda_1 = 400$ nm, ..., $\lambda_{31} = 700$ nm, and $\Delta\lambda = 10$ nm. The depth profile of PAR so obtained is shown by the solid line in Fig. 11.28. Note that the bottom of the euphotic zone, taken to be the depth at which PAR has decreased to 1% of it surface value, is $z_{eu} = 17$ m. The dashed line shows K_{PAR}, the diffuse attenuation coefficient for PAR.

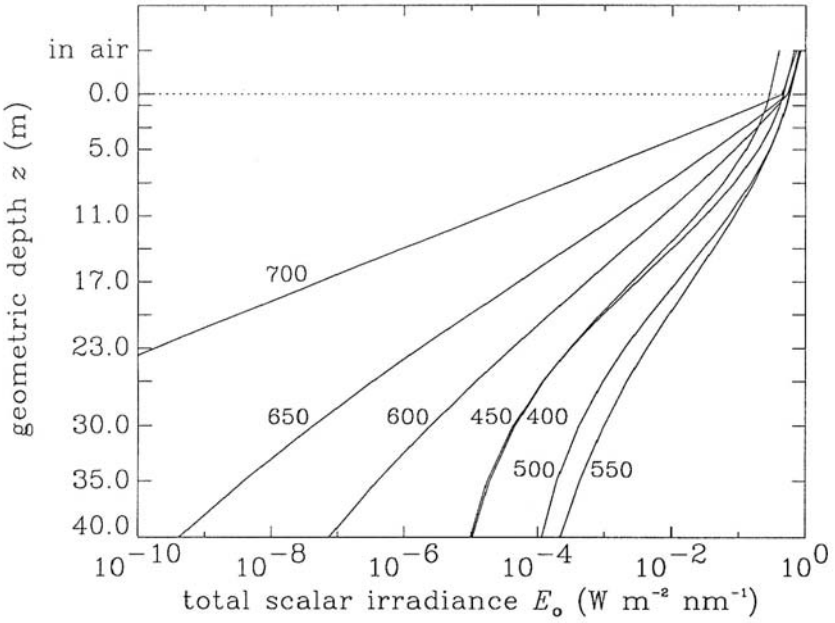

Fig. 11.26. The spectral total scalar irradiance $E_o(z;\lambda)$ as a function of depth for selected wavelengths.

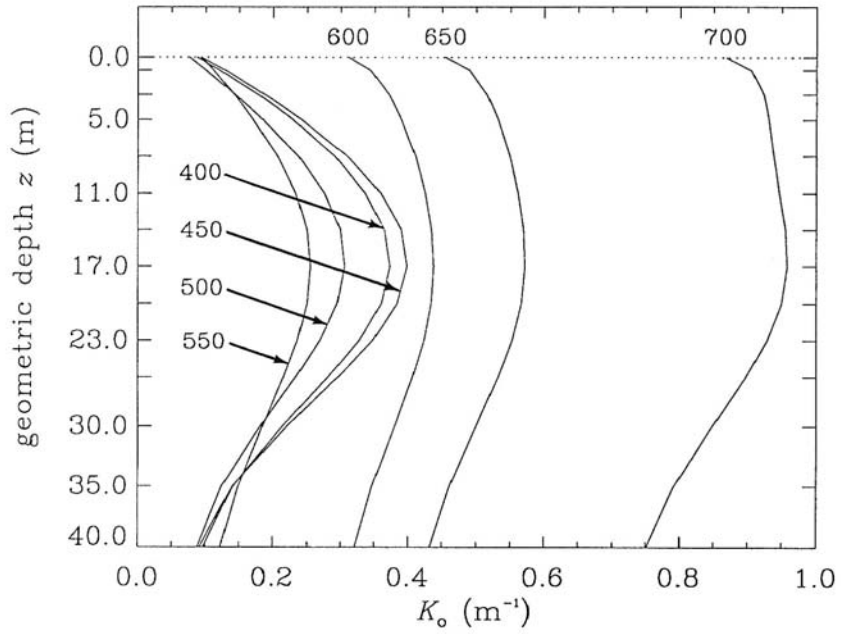

Fig. 11.27. Diffuse attenuation coefficients for spectral total scalar irradiance, $K_o(z;\lambda)$, corresponding to Fig. 11.26.

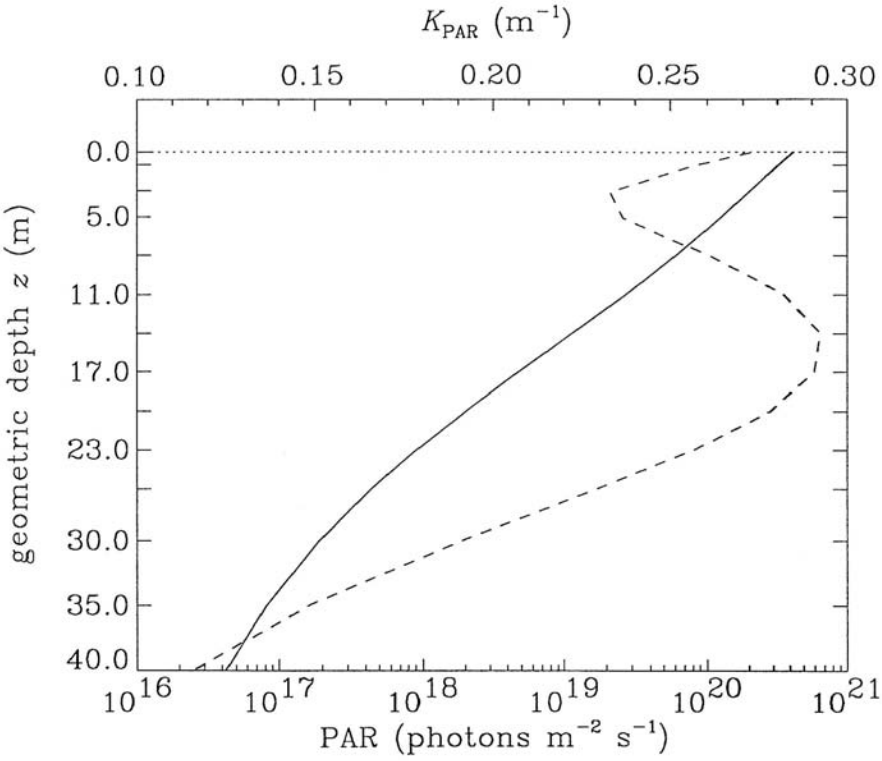

Fig. 11.28. The solid line and bottom abscissa give the photosynthetically available radiantion, PAR, as computed from $E_o(z;\lambda)$. The dashed line and upper abscissa give K_{PAR}, the diffuse attenuation coefficient for PAR.

Reflectances

Figure 11.29 shows the irradiance reflectance $R(z;\lambda) = E_u(z;\lambda)/E_d(z;\lambda)$ at selected depths. The curve labeled "in air" is $R(z=a;\lambda)$, which is the total albedo A of the water body. A includes the contribution to $E_u(a;\lambda)$ of direct-solar and diffuse-sky radiance reflected upward by the water surface itself. The albedo remains high at red wavelengths because of the surface reflectance. Within the water, R decreases greatly in the red, where the water is highly absorbing. Note the similarity in shape between $R(z;\lambda)$ and $\omega_o(z;\lambda)$, as seen in Fig. 11.22(b). The dotted line shows the asymptotic value $R(\infty)$, computed as in Eq. (9.86).

Figure 11.30 shows selected zenith (nadir-viewing) radiances. The curve labeled $L_u(z=w)$ is the zenith radiance just below the water surface, $L(z=w;\theta=180°,\cdot;\lambda)$. L_w is the water-leaving radiance just above the surface.

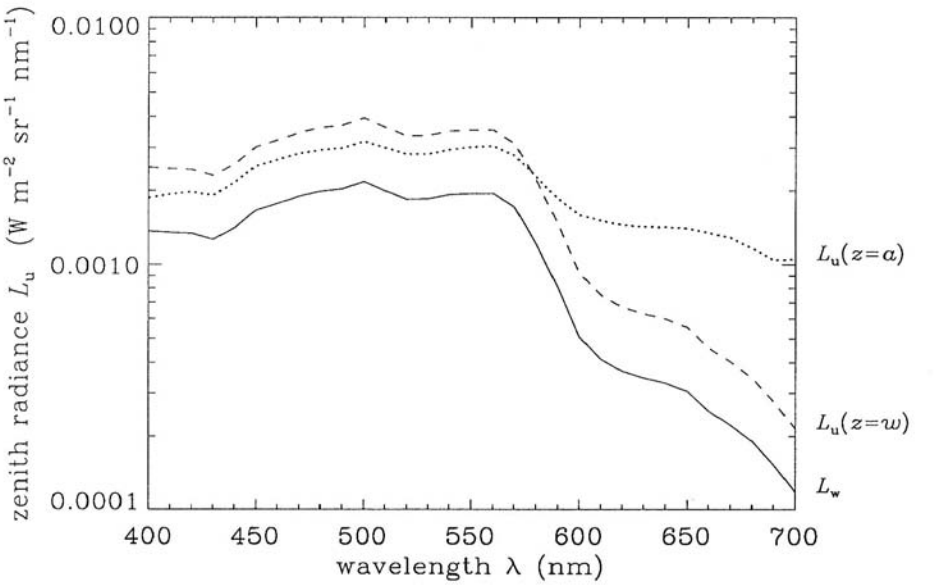

Fig. 11.29. Irradiance reflectance $R(z;\lambda)$ at selected depths. The curve labeled "in air" is $R(a;\lambda)$, the total albedo of the water body.

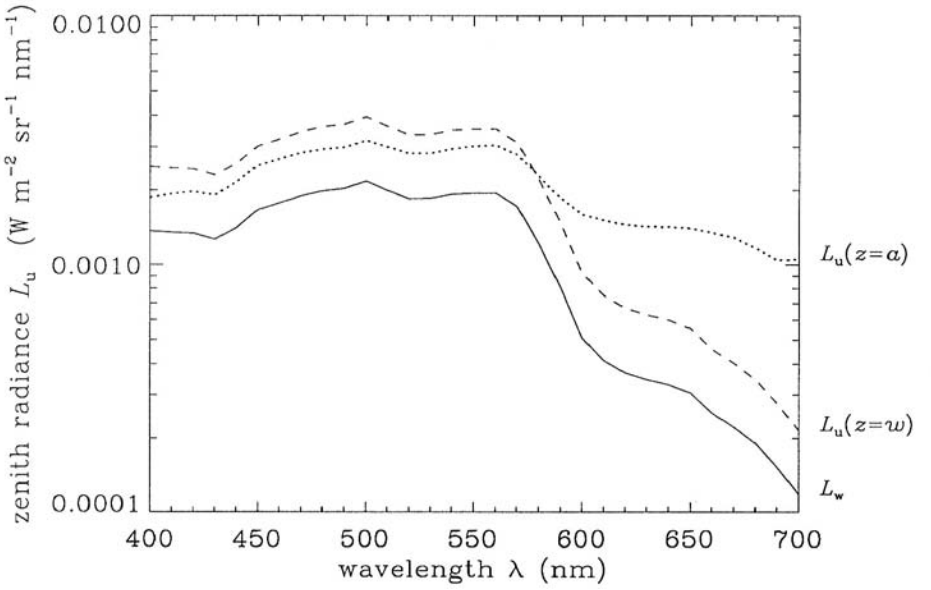

Fig. 11.30. Selected zenith (nadir-viewing) radiances. $L_u(z=w)$ is just below the air-water surface; $L_u(z=a)$ is just above the surface. L_w is the water-leaving radiance, which is $L_u(z=a)$ corrected for the surface reflectance of downwelling sky and solar radiance.

The $L_u(z=a)$ curve is the total zenith radiance in the air just above the surface. $L_u(z=a)$ includes both the water-leaving radiance L_w and the downwelling radiance from the sun and sky that is reflected upward into the zenith quad by the wind-blown water surface. $L_u(z=a)$ is the quantity actually measured by a nadir-viewing radiometer just above the sea surface.

A quick check on these plotted values is worthwhile. Let us assume that the effects of the wind-blown surface can be ignored, so that only the polar cap quads need be considered. Then the quad-averaged $L_u(z=w)$ and L_w are related by the n^2 law for radiance:

$$L_w = L_u(z=w) \frac{t(w,a;180,\cdot \rightarrow 180,\cdot)}{n_w^2} .$$

Substituting values from the figure at λ = 400 nm and using a Fresnel transmittance for normal incidence gives

$$0.0014 = 0.0025 \frac{0.98}{(1.34)^2} \approx 0.0014 \text{ W m}^{-2} \text{ sr}^{-1} \text{ nm}^{-1} .$$

For a wind-blown surface, radiance in all quads $Q_{rs} \in \Xi_u$ will contribute something to the water-leaving radiance in the zenith direction [recall Eq. (4.66)], but the zenith-quad-to-zenith-quad transfer explains most of the magnitude of L_w. The value of $L_u(z=a)$ is given approximately by L_w plus the nadir (zenith-viewing) sky radiance that is reflected upward by the surface:

$$L_u(z=a) \approx L_w + L_d(z=a)\, r(a,w;0,\cdot \rightarrow 180,\cdot) .$$

The value of $L_d(z=a)$, taken from the digital output, is 0.025 W m^{-2} sr^{-1} nm^{-1}. We thus have

$$0.0019 \approx 0.0014 + (0.025)(0.02) \approx 0.0019 \text{ W m}^{-2} \text{ sr}^{-1} \text{ nm}^{-1} .$$

Various remote-sensing reflectances $R_{rs}(z;\lambda)$ are shown in Fig. 11.31. The solid line gives $R_{rs}(a;\lambda) = L_w(\lambda)/E_d(a;\lambda)$ as customarily used in remote-sensing studies of ocean color. The three dashed lines give the same ratio, $L_u(z;\lambda)/E_d(z;\lambda)$, at selected depths within the water. The dotted line shows the (incorrect) value of $R_{rs}(a;\lambda)$ as obtained from $L_u(z=a)/E_d(z;\lambda)$. Comparing the dotted and solid lines shows the magnitude of the error in R_{rs} that can result from an improper removal of the sea-surface reflectance effects from measured $L_u(z=a)$ values.

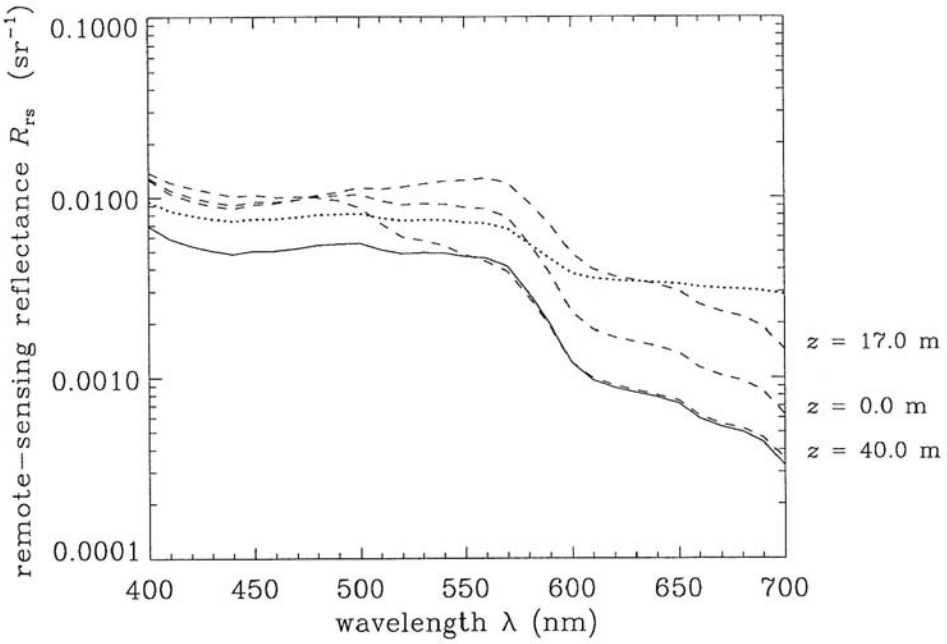

Fig. 11.31. Remote-sensing reflectances. The solid line is $R_{rs} = L_w(\lambda)/E_d(a;\lambda)$, as usually defined. The dashed lines are the ratio $L_u(z;\lambda)/E_d(z;\lambda)$ at selected depths within the water. The dotted line is $L_u(a;\lambda)/E_d(a;\lambda)$, where $L_u(a;\lambda)$ includes surface-reflectance effects.

Average cosines

The average cosines of the downwelling ($\bar{\mu}_d$) and upwelling ($\bar{\mu}_u$) light fields are shown as solid lines in Fig. 11.32. The average cosine $\bar{\mu}$ of the entire light field is shown as dashed lines. The wavelengths are 400, 450,...,700 nm, as in previous plots of this format. The $\bar{\mu}_u$ values are quite uniform throughout the water column, even for this highly stratified water body. The value $\bar{\mu}_u \approx 3/8$ mentioned in Section 3.2 is a good approximation to the actual values. The values of $\bar{\mu}_d$ and $\bar{\mu}$ show a somewhat more complicated depth behavior, especially in the red.

The asymptotic values of $\bar{\mu}_u$ vary only slightly with wavelength; the extreme values are $\bar{\mu}_u(\infty) = 0.3718$ at $\lambda = 560$ nm and $\bar{\mu}_u(\infty) = 0.3945$ at $\lambda =$ 400 nm. Values of $\bar{\mu}_d(\infty)$ vary from 0.7069 at $\lambda = 400$ nm to 0.9343 at $= 700$ nm.

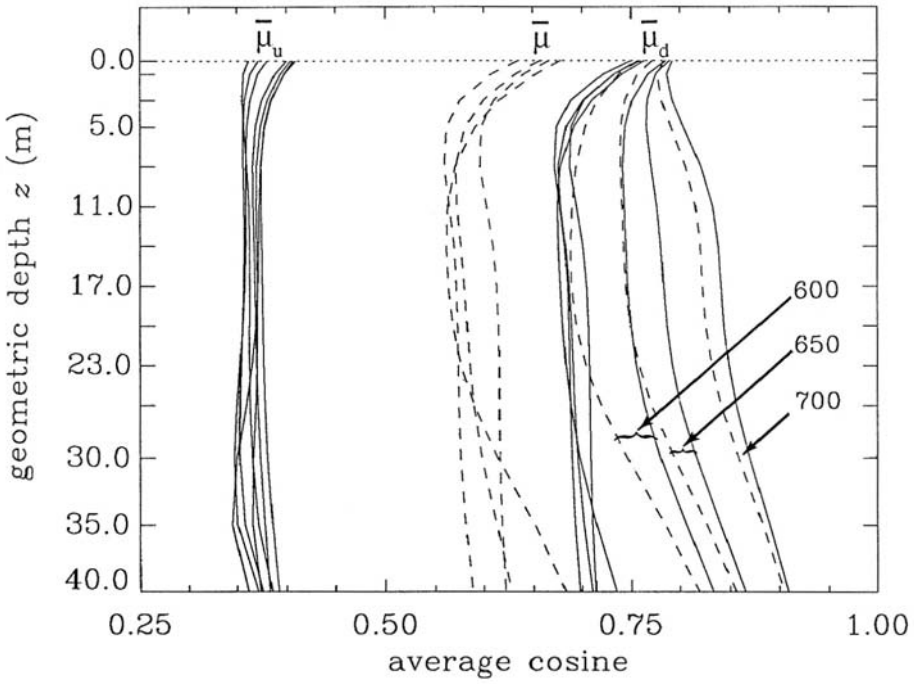

Fig. 11.32. Average cosines for the downwelling ($\bar{\mu}_d$, solid lines), upwelling ($\bar{\mu}_u$, solid lines), and total ($\bar{\mu}$, dashed lines) light fields, for the same selected wavelengths as in the previous figures of this format.

11.9 Problems

11.1 Figure 11.10 shows radiance distributions just above and just below the air-water surface. Depending on the viewing angle, either the air or water radiance is greater. Qualitatively explain this behavior in terms of the n^2 law for radiance, the Fresnel reflectance of the surface, the sky radiance distribution, and so on. First consider viewing angles in the ϕ_v half plane near the nadir [$L(\zeta=w) > L(\zeta=a)$], and near the zenith [$L(\zeta=w) < L(\zeta=a)$]. Repeat for the ϕ_v half plane.

11.2. Discuss how you would include bubbles in a numerical model, in order to simulate the situation seen in Fig. 11.11. Consider Eqs. (3.10)-(3.13), the discussion of Section 3.11, and perhaps even the paper by Wu (1988) in answering this question.

11.3. In Eqs. (11.3) and (11.4), we expressed the K_d values associated with Fig. 11.15 in nondimensional form, i.e. the derivatives were taken with respect to optical depth.
(a) Convert these $\boldsymbol{K_d^{nd}}$ values into their customary dimensional values.
(b) In part (a) you should have found that the dimensional $K_d(\zeta=15) > K_d(\zeta=5)$ for both panels of Fig. 11.15. This seems to contradict Eq. (11.4) and Fig. 11.15(b), which has $\boldsymbol{K_d^{nd}(15) < K_d^{nd}(5)}$. Explain how the highly scattering layer of Fig. 11.15(b) can cause E_d to decay less rapidly with optical depth but more rapidly with geometric depth.

11.4. Use the water-leaving radiance shown in Fig. 11.30, and Fig. 10.2, to recover the chlorophyll concentration of the Celtic Sea. How does the "remotely sensed" value of C compare with the "measured" profile seen in Fig. 11.18?

11.5 How does the depth of the euphotic zone as obtained from Fig. 11.28 compare with z_{eu} as determined from Table 3.18, using an average value of C estimated from Fig. 11.18?

Epilogue

As I worked on this book in a desultory fashion over the years, two quotes kept coming to mind. The first, by Wilson Mizner, says,"When you steal from one author, it's plagiarism; if you steal from many, it's research." I can only hope that my effort here in synthesizing the work of so many scientists will also be viewed as a worthy contribution to hydrologic optics. The second quote is by an anonymous woodworker. When asked how he decided that he was done polishing a newly finished piece of furniture, he replied, "Its never done, but one day they just come and take it away." And so it is with the present book. My funding has run out, new adventures await, and what has been written so far is of more value in the readers' hands than on my desk awaiting further polishing.

All wordprocessing, including layout of the camera-ready copy, was done using WordPerfect® 5.1 for UNIX Systems, a product of WordPerfect Corporation. Computer-generated figures, such as those seen in Chapter 11, were drawn using IDL® (Interactive Data Language), a product of Research Systems, Inc. Printout was generated with PostScript® fonts, a product of Adobe Systems, Inc., on a QMS PS815 printer, a product of QMS, Inc. Numerical modeling was carried out in FORTRAN 77 on a SPARCstation® 2, a product of Sun Microsystems, Inc.

References >>

<< Table of Contents